Check for updates

AGU ADVANCING EARTH AND SPACE SCIENCE

Water Resources Research

RESEARCH ARTICLE

10.1029/2020WR028671

A Systematic Investigation Into the Control of Roughness on the Flow Properties of 3D-Printed Fractures

Tomos Phillips[1,2], Tom Bultreys[2], Kevin Bisdom[3], Niko Kampman[3], Stefanie Van Offenwert[2], Arjen Mascini[2], Veerle Cnudde[2,4], and Andreas Busch[1]

[1]Institute of GeoEnergy Engineering, Heriot-Watt University, The Lyell Centre, Edinburgh, UK, [2]Department of Geology, PProGRess/UGCT, Ghent University, Ghent, Belgium, [3]Shell Global Solutions International B.V., Amsterdam, The Netherlands, [4]Department of Earth Sciences, Utrecht University, Utrecht, The Netherlands

Key Points:

- We systematically investigate the control of fracture surface roughness on the fluid flow properties of 3D-printed fractures
- Stress-dependent aperture structure evolution was imaged using laboratory-based micro-CT
- For fracture apertures <~20 μm, contact area is more effective than surface roughness when predicting stress-dependent permeability

Supporting Information:

Supporting Information may be found in the online version of this article.

Correspondence to:

T. Phillips,
tp45@hw.ac.uk

Citation:

Phillips, T., Bultreys, T., Bisdom, K., Kampman, N., Van Offenwert, S., Mascini, A., et al. (2021). A systematic investigation into the control of roughness on the flow properties of 3D-printed fractures. *Water Resources Research*, *57*, e2020WR028671. https://doi.org/10.1029/2020WR028671

Received 25 AUG 2020
Accepted 21 MAR 2021

Author Contributions:

Conceptualization: Tomos Phillips, Niko Kampman, Arjen Mascini
Data curation: Tomos Phillips
Formal analysis: Tomos Phillips, Kevin Bisdom
Funding acquisition: Arjen Mascini, Veerle Cnudde
Investigation: Tomos Phillips, Stefanie Van Offenwert, Andreas Busch
Methodology: Tomos Phillips, Tom Bultreys, Niko Kampman, Arjen Mascini
Project Administration: Arjen Mascini, Veerle Cnudde

© 2021. The Authors.
This is an open access article under the terms of the Creative Commons Attribution License, which permits use, distribution and reproduction in any medium, provided the original work is properly cited.

Abstract Heterogeneous fracture aperture distribution, dictated by surface roughness, mechanical rock and fracture properties, and effective stress, limits the predictive capabilities of many reservoir-scale models that commonly assume smooth fracture walls. Numerous experimental studies have probed key hydromechanical responses in single fractures; however, many are constrained by difficulties associated with sample preparation and quantitative roughness characterization. Here, we systematically examine the effect of roughness on fluid flow properties by 3D printing seven self-affine fractures, each with controlled roughness distributions akin to those observed in nature. Photogrammetric microscopy was employed to validate the 3D topology of each printed fracture surface, enabling quantification using traditional roughness metrics, namely the Joint Roughness Coefficient (*JRC*). Core-flooding experiments performed on each fracture across eight incremental confining pressure increases (11–25 bar), shows smoother fractures ($JRC < 5.5$) exhibit minor permeability variation, whilst rougher fractures ($JRC > 7$) show as much as a 219% permeability increase. Micro-computed tomography imaging of the roughest fracture under varying effective stresses (5–13.8 bar), coupled with inspection into the degree of similarity between fracture closure behavior in 3D-printed and natural rock fractures, highlight the capabilities of 3D-printed materials to act as useful analogs to natural rocks. Comparison of experimental data to existing empirical aperture-permeability models demonstrates that fracture contact area is a better permeability predictor than roughness when the mechanical aperture is below ~20 μm. Such findings are relevant for models incorporating the effects of heterogeneous aperture structures and applied stress to predict fracture flow in the deep subsurface.

Plain Language Summary Stark permeability contrasts between fractures and surrounding rock make them a critical feature governing heat and mass transport in the Earth's subsurface, while also playing an integral role in many natural processes and subsurface engineering applications. A fractures aperture (void space) determines its fluid transport capabilities, making this crucial information needed to inform numerical models seeking to predict flow rates across many scales (centimeters to kilometers). For simplicity, common fracture representations equate the effective (hydraulic) and geometric (mechanical) apertures (i.e., perfectly smooth walls). In nature, all rock fractures display rough walls to various degrees, limiting the predictive capabilities of smooth-walled models. Here, we performed fluid flow experiments on 3D-printed fractures with controlled surface roughness to investigate the effect on fluid transport. We find that roughness enables the persistence of void space, which enhances fluid flow. High-resolution imaging shows that below ~20 μm, the influence of fracture contact area on permeability is greater than roughness. Such findings are relevant for fracture flow models attempting to incorporate the effect of heterogeneous apertures and applied stress on fluid flow properties in fractures, which is important in the deep subsurface where applied stresses force fluid to navigate discrete contact points between opposing fracture walls.

1. Introduction

Fluid transport through rock fractures underlies many natural processes, such as fault rupture (Faulkner et al., 2010), while also influencing hydrocarbon production (Austad et al., 2012; Godec et al., 2013), geothermal heat extraction (Martínez et al., 2014), temporary energy storage (e.g., H_2) (Kabuth et al., 2017; McCartney et al., 2016), and long-term nuclear and anthropogenic waste storage (e.g., CO_2) (Z.-Q. Huang

Resources: Kevin Bisdom, Niko Kampman, Arjen Mascini, Veerle Cnudde
Software: Tom Bultreys, Kevin Bisdom, Niko Kampman
Supervision: Tom Bultreys, Niko Kampman, Arjen Mascini, Veerle Cnudde
Validation: Tomos Phillips, Tom Bultreys, Kevin Bisdom, Arjen Mascini
Visualization: Tomos Phillips
Writing – original draft: Tomos Phillips
Writing – review & editing: Tom Bultreys, Kevin Bisdom, Arjen Mascini, Veerle Cnudde

et al., 2015; Pruess, 2008). Fluid flow in single fractures is dictated by aperture distribution, which is underpinned by the geometrical and chemical heterogeneity of the wall rock, and the coupling of flow and effective stress, σ' (C. A. Barton et al., 1995; Berkowitz, 2002; Y. W. Tsang & Witherspoon, 1981). An improved understanding of single-fracture scale hydromechanics, and resulting implications on fracture network- and reservoir-scale transport capabilities, is required for continued and future comprehension of fractured media (Phillips et al., 2020).

Natural fracture surfaces exhibit deviations from planarity in the form of asperities, termed roughness (Adler et al., 2012; Grasselli et al., 2002; Y. Li & Huang, 2015), which has varying impacts on flow depending on the scale of consideration (i.e., first-order waviness and second-order unevenness) (cf. Dou et al., 2019; M. Wang, Chen, et al., 2016; Zou et al., 2015). Discrete roughness promotes heterogeneous apertures and complex flow properties (Brown & Scholz, 1985a; Pyrak-Nolte et al., 1988; C. F. Tsang & Neretnieks, 1998), commonly motivating a perfectly smooth parallel plate idealization (e.g., Thompson & Brown, 1991; Unger & Mase, 1993), described by the cubic law, CL (Snow, 1969; Witherspoon et al., 1980):

$$Q = -\frac{wa^3}{12\eta}\Delta P \tag{1}$$

where Q ($\mathrm{m^3\,s^{-1}}$) is the volumetric flow rate, w (m) is the fracture width, a (m) is the aperture, η (Pa s) is the fluid viscosity, and ΔP (Pa) is the fluid pressure gradient.

Reservoir-scale models predominantly assume smooth-walls when representing fractures discretely to obtain bulk flow properties (Latham et al., 2013; Long et al., 1982; Luo et al., 2016). Numerical (e.g., Ai-Yaarubi et al., 2005; Boutt et al., 2006; Brush & Thomson, 2003; Crandall, Ahmadi, & Smith, 2010; Ge, 1997; Glover et al., 1997; Karimzade et al., 2019; Konzuk & Kueper, 2004; Liu et al., 2020; Oron & Berkowitz, 1998; Yeo et al., 1998; Zimmerman & Yeo, 2000; Zimmerman et al., 2004) and experimental studies (e.g., Brace, 1980; Brown, 1987; Z. Chen et al., 2017; Durham & Bonner, 1994; Nicholl et al., 1999; Piggott & Elsworth, 1990; Plouraboue et al., 2000; Pyrak-Nolte et al., 1987; Qian et al., 2005, 2011; Raven & Gale, 1985; Rong et al., 2020; Tan et al., 2020; Y. W. Tsang & Tsang, 1990) demonstrate the sensitivity of flow to aperture and roughness, highlighting the CL's shortcomings in predicting single-fracture permeability, k^f. Constricted advective flow is resolved by assigning a (effective) hydraulic aperture, e_h, which always appears smaller than the mechanical aperture, e_m, representing the geometric mean between opposing surfaces (Esaki et al., 1999; Hakami & Larsson, 1996; Klimczak et al., 2010). Our limited understanding of this reduced aperture hinders model predictions (Vogler et al., 2018; Zimmerman & Bodvarsson, 1996).

Stress-induced aperture decrease further complicates flow properties by increasing fracture contact area, R_c, which enhances flow tortuosity and preferential flows (Briggs et al., 2017; Brown et al., 1998; de Dreuzy et al., 2012; Y. W. Tsang & Tsang, 1989; Watanabe et al., 2009; F. Xiong et al., 2018; Zou & Cvetkovic, 2020). Such behavior is commonly described by fracture normal stiffness, k_n, a geometry-dependent mechanical property describing the ratio of change in σ' versus aperture, which has been widely used to characterize stress-dependent closure (Bandis et al., 1983; Goodman et al., 1968; Hopkins, 2000; Hopkins et al., 1990; Petrovitch et al., 2013; Pyrak-Nolte & Morris, 2000; Pyrak-Nolte & Nolte, 2016; L. Wang & Cardenas, 2016). These studies highlight the importance of R_c and resulting spatial aperture distribution in governing k^f. Other studies identifying the need for practical k_n characterization, with limited data over a small stress range, proposed a stiffness characteristic, $\chi = \mathrm{d}k_n/\mathrm{d}\sigma'$, where the curve of k_n versus σ' is linear with slope χ, completely describing stress-dependent closure (Evans et al., 1992; Zangerl et al., 2008).

In the subsurface, roughness and R_c are typically unknown, meaning resolving their impact on flow is primarily reliant on laboratory-scale studies to guide simulations and conceptual models. However, as fracture properties are heterogeneous and anisotropic (Bisdom et al., 2016; Laubach et al., 2018), investigating their impact on flow within a specific rock volume, repeatedly and consistently, is inherently challenging. Therefore, despite advancements in our understanding of single-fracture flow, previous experimental efforts are constrained, in part, by difficulties associated with experimental repeatability, sample preparation (e.g., fragmentation during coring) and quantitative roughness characterization (e.g., sample size vs. resolution). A more robust framework that provides an improved basis of the primary fracture properties governing k^f

is desirable, which, in turn, can be used to refine numerical models and provide alternative pathways of (back-)calculating subsurface k^f.

One avenue to address such challenges is three-dimensional printing (3DP), a rapid prototyping method capable of producing complex 3D objects from computer-aided-design (CAD) geometries (Piovesan et al., 2019). This rapidly evolving technique, coupled with digital rock physics, render this an increasingly popular method to investigate properties akin to natural rocks (e.g., Gomez et al., 2018; Hasiuk et al., 2018; Ishutov et al., 2015; Ishutov et al., 2017; Ju et al., 2014; Sharafisafa et al., 2018; Suzuki et al., 2017; Yazdi et al., 2016; Zhu et al., 2018). 3DP can therefore alleviate some uncertainties associated with natural rocks, facilitating systematic investigation into the control of micro/macroscopic heterogeneities on flow properties, thereby bridging the gap between laboratory tests and numerical simulations.

Recent 3DP studies investigated shear response (and asperity degradation) (Ishibashi et al., 2020) and non-Darcian flow regimes (Yin et al., 2020) in polymeric rough fractures. Attempts to more accurately replicate natural fracture material properties produced 3DP fracture replicas that were later molded into concrete (Q. Jiang, Feng, Gong, et al., 2016; Ni et al., 2018) or natural minerals (Fang et al., 2018). However, replicating fractures using higher strength materials is resolution-limited. Additional studies investigated other 3DP materials to further elucidate the geomechanical comparability to natural rocks (e.g., Barbosa et al., 2020; Fereshtenejad & Song, 2016; C. Jiang & Zhao, 2015; Q. Jiang, Feng, Song, et al., 2016; Kong et al., 2018; Vogler et al., 2017), indicating that absolute elastic properties (Young's modulus, Poisson's ratio and unconfined compressive strength [UCS]) vary from those found in the majority of natural rocks (e.g., UCS 30–90 MPa). Despite this, Zhou and Zhu (2018) identified a polymeric resin printed via stereolithography (SLA) as the most suitable material for mimicking rock mechanical behavior. This method, therefore, presents unique opportunities to generate high-resolution roughness while also enabling investigation into aperture structure heterogeneity under geological conditions, such as σ', which is key for subsurface flow predictions in rough fractures undergoing fluid pressure changes.

Here, we 3DP seven synthetic fractures with varying roughness distributions using an SLA-printed polymeric material. We verified the roughness and performed single-phase (steady-state) fluid flow experiments on each fracture to systematically investigate the effect of roughness on k^f with increasing σ'. X-ray micro-computed tomography (μ-CT) imaging was then performed on the roughest fracture during loading to visualize aperture evolution in a non-destructive manner.

2. Materials and Methods

2.1. Sample Generation and Preparation

A range of roughness distributions were fabricated by systematically varying the digital fractal dimension, D_f (−) (between 1.2 and 2.4), in seven sets of numerically designed fractures to produce seven self-affine Fracture Realizations (*FR#1–FR#7*, Figure 1a) with varying small-scale (second-order) roughness distributions. These synthetic surfaces were generated using *Synfrac*, which enabled the fabrication of two opposing rough fracture surfaces through accounting for complex matching properties and anisotropies within the defining properties of a fracture surface (cf. Brown, 1995; Isakov et al., 2001; Ogilvie et al., 2003). This (fractal) generation method (cf. Text S5 in the supporting information [SI]) has been shown to approximate natural rock fracture surfaces (e.g., Brown & Scholz, 1985b; Candela et al., 2012; Renard et al., 2013). To complement and investigate the efficacy of using 3DP fractures as natural rock fracture proxies, three Test Fractures (*TF#1–TF#3*) were also produced. A summary of the respective samples, and corresponding experiments performed, are detailed in Table S1 and Text S4.

2.2. 3DP Procedure

Following numerical generation, fracture sets were imported as equal size XYZ Cartesian point clouds into the 3D CAD software, *Rhinoceros6®*. Each surface was converted into a closed (watertight) polysurface to satisfy 3DP criteria. Each sample comprised two half-cylinders (Figures 1b and 1c; example of one fracture surface), acting as opposing fracture walls (top and bottom surfaces), that when assembled produced a

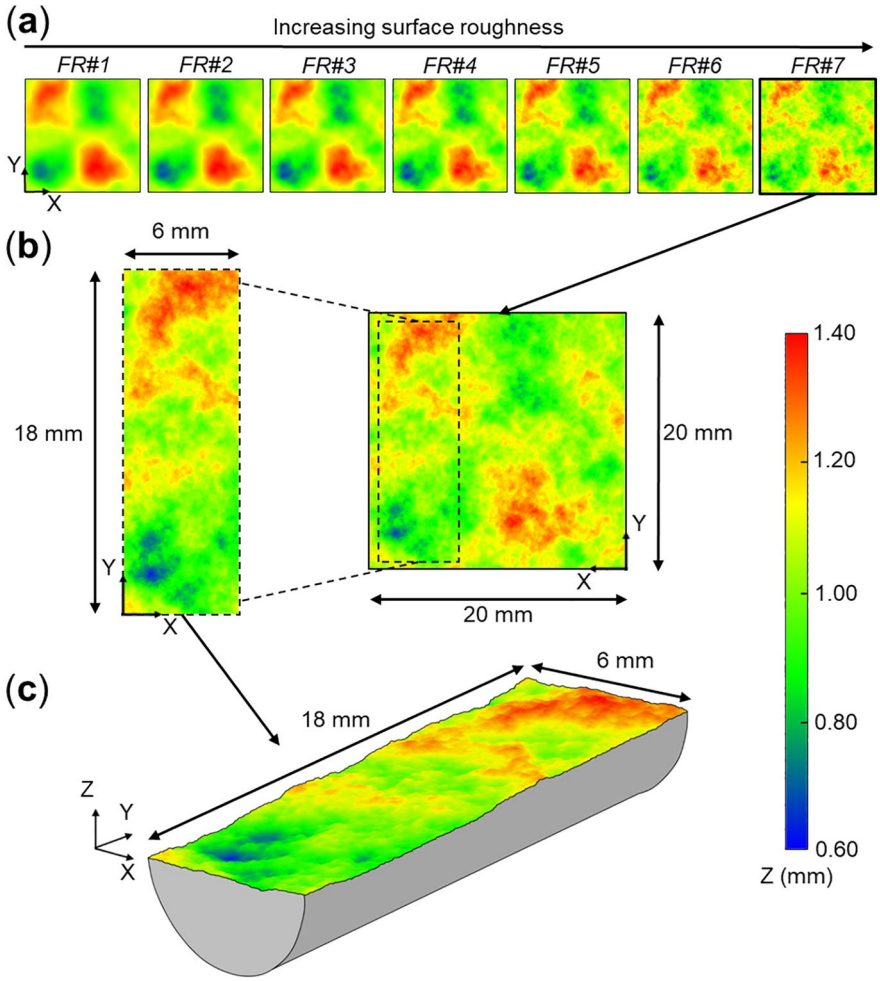

Figure 1. Workflow to 3D print fractures with different surface roughness distributions. (a) Primary suite of numerically generated synthetic fracture surfaces, increasing in roughness from *FR#1* (smoothest) to *FR#7* (roughest). (b) Enlarged view of *FR#7*, highlighting the region (dashed rectangle) selected for final fracture assembly shown in (c). (c) 3D view of the final part, comprising the half-cylinder and fracture (cf. Figure S1b for photograph). Note that the workflow depicted in (b and c) was repeated for each fracture surface, with details of this provided in Text S1, accompanied by all top and bottom fracture surfaces (Figure S2).

single fracture measuring 18 mm in length and 6 mm diameter. Details on the opposing fracture surface alignment protocol are provided in Text S5 and Figure S7.

A repeatability test, using two digitally identical fractures (*TF#2, TF#3*), was performed to investigate the reproducibility of top and bottom surfaces using identical build and print specifications. Through 2D amplitude roughness analysis (Gadelmawla et al., 2002; Stout, 2000), this test was deemed satisfactory, yielding differences as low as 1.6% between each fracture (cf. Text S4).

All fractures were printed with a *Formlabs®2* 3D printer, using a clear photopolymer Acrylonitrile Butadiene Styrene (ABS) resin (cf. Table S2 for material properties) (Formlabs, 2019). Printing was accomplished using SLA methods, where an ultraviolet laser cured each resin layer to produce the desired 3D part. Of the 3DP methods reported below, this yielded the highest resolution whilst being readily affordable and available. Other methods were investigated, namely *Accura® Xtreme™* tough-resin, printed using a *ProJet® 7000* printer. Surface roughness comparisons between *Accura® Xtreme™* and ABS were performed, with the former yielding lower resolution and was therefore not selected. The reported resolution of the chosen printer was 25 μm in the *x*-direction, 50 μm in the *y*-direction, and 100 μm in the *z*-direction, operating with a laser

spot size of 140 μm. This resolution was higher than that of the final digital fracture surfaces (cf. Text S1), suggesting microscopic roughness distributions could be fully resolved during printing.

2.3. Surface Roughness Characterization

We characterized the roughness of each fracture surface using digital optical microscopy to verify that the printed samples were representative of their model counterparts and to enable robust comparison between fractures. An automated image processing workflow, written in *Python*™, was designed to alleviate user interpretation bias, making use of scikit-image algorithms (van der Walt et al., 2014). The following broadly describes the experimental setup and metrics used to quantify surface roughness. Detailed information on the experimental workflow and functionality of the data processing code is provided in Text S2 and S3.

2.3.1. Digital Optical Microscopy

A *Keyence® VHX™-6000* digital optical microscope (Keyence, 2017) was used to investigate (micrometer-scale) roughness distributions of each 3DP fracture surface in a non-destructive manner (Figure S3). This surface-imaging tool utilized photogrammetry to obtain 3D spatial information (x-, y-, and z-co-ordinates) of each surface. The maximum image size was 20,000 × 20,000 pixels, resulting in a resolution of ~1–2.5 μm per pixel at 100x magnification. This method calculated the surface height over a 2D grid by compiling multiple partially overlapping images at different exposures and focal planes.

2.3.2. Surface Roughness Analysis

We quantified the roughness of each fracture surface using widely adopted 1D dimensionless metrics for quantifying natural fracture surface roughness, namely the Joint Roughness Coefficient, *JRC* (−), (cf. N. Barton & Choubey, 1977; C. A. Barton et al., 1985) and the root mean square of the first derivative of the fracture surface profile, Z_2 (−), (cf. Tse & Cruden, 1979). Experimental studies on roughness have discussed empirical relations between *JRC* and Z_2 (cf. Y. Li & Zhang, 2015; Yu & Vayssade, 1991). Here, for a 1D profile comprising equally spaced points, we used the relation by Y. Li and Zhang (2015):

$$JRC = 98.718 \cdot Z_2^{1.6833} \tag{2}$$

where Z_2 is expressed discretely as (Myers, 1962):

$$Z_2 = \left[\frac{1}{N_t} \Sigma \left(\frac{Z_{i-1} - Z_i}{x_{i-1} - x_i} \right)^2 \right]^{1/2} \tag{3}$$

where x_i and Z_i denote surface profile co-ordinates, and N_t the number of sampling points along the fracture length. The *JRC*, ranging between 0 (perfectly smooth) and 20 (high roughness) (N. Barton & Choubey, 1977), can be used to compare mechanical and hydraulic fracture properties with regard to surface roughness variations and is a direct input parameter for k^f models (Olsson & Barton, 2001). We calculated these metrics by analyzing each row and column of pixels in the 2D fracture height matrix as separate 1D-roughness profiles, which yielded Z_2 measures in x- and y-directions and enabled determination of mean Z_2 and *JRC*'s in both horizontal directions.

The similarity between the 3DP fractures and their digital counterparts were investigated using the Hurst coefficient, H (−) (cf. Text S4), a measure of self-affinity (Adler et al., 2012). All printed surfaces were within a 10% range of the digital models (cf. Figure S6).

2.4. Experimental Fluid Flow Setup

2.4.1. Single-Phase Flow Procedure

Single-phase permeability measurements were conducted on *FR#1–FR#7* using a custom-built, Hassler-type PEEK flow cell (Figure 2a). Samples were placed in a *Viton®* sleeve (Figure 2b) before applying an isotropic confining pressure, P_c (bar), with water as the confining fluid. A *Vindum Engineering VP-12K* piston pump continuously injected (0.01 mL/min; ±0.01% of set point) deionized water into the sample inlet, while P_c

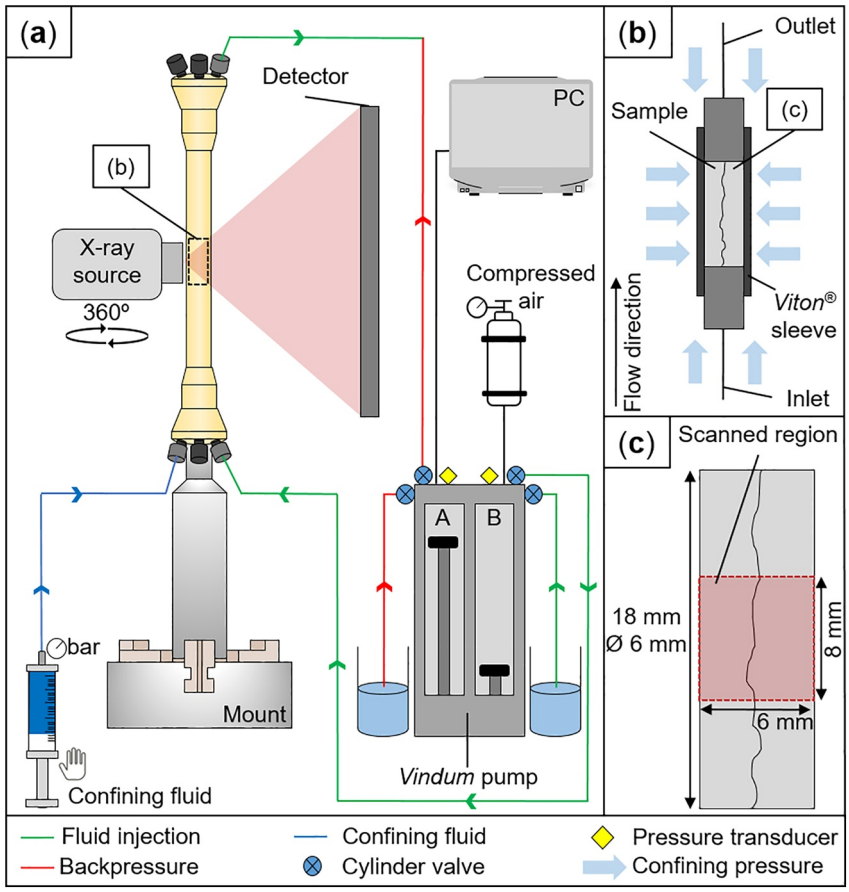

Figure 2. Experimental apparatus. (a) Schematic experimental flow setup. (b) Enlarged view of the region highlighted in (a), showing isotropic confinement. (c) Enlarged view of the sample shown in (b), denoting which subsection was imaged with μ-CT (cf. Section 2.5). μ-CT, micro-computed tomography.

was incrementally increased eight times for each sample (from 11 to 25 bar). Maintaining a constant flow rate while modifying P_c resulted in alterations in the mean pore pressure, P_p (bar), which enabled permeability investigation across a range of σ' ($\sigma' = P_c – P_p$, ~12.5 bar).

For consistency, and to enable direct comparison between samples, a repeatable and consistent procedure was adopted. Once mounted in the flow cell, 11 bar of P_c was applied to the sample for 30 min to ensure sleeve integrity. A downstream pore-fluid pressure of 5 bar was introduced, followed by 5 bar of pore-fluid pressure on the upstream. Fluid was continuously injected (0.01 mL/min) at room temperature (20 °C ± 0.5 °C). Once the pressure drop, ΔP, over the sample stabilized (i.e., steady-state), two on-board pressure transducers (error ± 12 kPa) (Figure 2a) recorded ΔP at each P_c step with a sampling frequency of 15 s for 30 min, yielding 120 data points from which average upstream and downstream pressures were calculated. For the full P_c range, the materials sensitivity to creep was tested, and k^f was deemed to be within an acceptable range after ~20 min. Therefore, samples were pre-loaded for 30 min prior to ΔP recording began to avoid the influence of plastic deformation (*TF#1*; Text S4).

2.4.2. Fracture Permeability and Hydraulic Aperture Quantification

The sample permeability, k^s (m^2), was calculated for each P_c step using Darcy's law (Darcy, 1856):

$$k^s = -\frac{\eta L Q}{A \Delta P} \tag{4}$$

where L (m) and A (m^2) are the sample length and cross-sectional area, respectively. Injection rates and σ' ranges were selected to only investigate laminar (Darcian) flow, applicable to the majority of geological flows (Council, 1996), so a Reynolds number, Re (−), <1. We calculated Re via (Zimmerman et al., 2004):

$$Re = \frac{\rho Q}{\eta w} \tag{5}$$

where ρ (kg m^3) is the fluid density. All Re were within the laminar flow regime ($Re < 3.1 \times 10^{-2}$), validating the use of Equation 4 (Konzuk & Kueper, 2004).

e_h (m) was quantified through analysis of Q and ΔP, which exhibited a linear relationship for all samples (Brown, 1987; Z. Chen et al., 2000; Matsuki et al., 2006):

$$e_h = \left(\frac{12\eta Q}{w\left(\Delta P \,/\, L\right)} \right)^{1/3} \tag{6}$$

This enabled k^f (m^2) to be calculated as (Watanabe et al., 2008; Witherspoon et al., 1980):

$$k^f = \frac{e_h^2}{12} \tag{7}$$

2.5. Laboratory-Based μ-CT

We performed μ-CT imaging on the roughest fracture to visualize aperture evolution with increasing σ'. For this, we printed a replica of *FR#7* (*FR#7_2*; Table S1). The experimental setup, and parameters investigated, are detailed in the following.

2.5.1. Experiment Description

Laboratory-based μ-CT was used to image single-phase fluid flow through *FR#7_2*. This allowed for non-destructive (micrometer-scale) aperture visualisation through capturing the X-ray attenuation contrast between the 3DP sample and fracture (Heindel, 2011; Ketcham et al., 2010).

Contrasting the (nonimaged) fluid flow experiments performed on *FR#1 – FR#7*, a tagged brine solution (5 wt. % potassium iodide) was used as the permeating fluid to enhance contrast between the fracture and ABS material. Scans were undertaken using a gantry-based environmental μ-CT (EMCT) system (Bultreys et al., 2016), which enabled the sample, flow cell, wires, and tubing to remain static while the X-ray source and detector rotated 360° freely (Figure 2a). Four scans at different σ''s (cf. Table 1) were executed to investigate aperture evolution during fracture closure, $-\Delta e_m$ (μm). The process for mounting the sample in the flow cell, applying P_c and backpressure, and continuously injecting fluid into the fracture was the same as described in Section 2.4.1. A flow rate of 0.073 mL/min was favored as aperture was more easily resolved than when operating at a lower flow rate of 0.01 mL/min.

2.5.2. Mechanical Aperture Quantification

Acquired μ-CT radiographs were reconstructed using *Octopus Reconstruction* (Vlassenbroeck et al., 2007), while *Avizo*^{TM} *(Thermo Fischer Scientific)* was used to analyze reconstructed image slices in 3D. For each experiment, multiple scans recorded at different locations along the samples vertical axis were stitched together to obtain a total image size of 6 × 6 × 8 mm, corresponding approximately to the sample center (Figure 2c). For image denoising, a non-local means edge-preserving filter was applied to the reconstructed volumes (Buades et al., 2005, 2008). The fracture was then distinguished from the surrounding material (ABS sample and *Viton*® sleeve) through watershed segmentation in *Avizo*^{TM} (Schlüter et al., 2014). Following segmentation, direct volume renderings of e_m at each σ' were generated, and fracture volumes, k^f_{vol} (mm^3), were computed. e_m for each σ' was then estimated using a Euclidean distance transform, producing an XYZ scalar field with floating-point values from which local thicknesses were extracted to plot e_m distribution

Table 1
Scan Settings and Test Parameters for Each μ-CT Experiment Performed on Sample FR#7_2

Experiment setting	Scan no. 1	Scan no. 2	Scan no. 3	Scan no. 4
Confining pressure (P_c) (bar)	11	16	21	24
Effective stress (σ') (bar)	5	9.2	12.8	13.8
Voxel size (μm)		5.76		
Exposure time (ms)		160		
Tube power (W)		8		
Tube voltage (kV)		70		
Amount of projections per full rotation (−)		2,201		
Acquisition time (min)		30		
Scans per series (−)		1		
No. of averages (−)		5		

Abbreviation: μ-CT, micro-computed tomography.

maps and frequencies. The mean e_m was calculated by dividing the total k^f_{vol} of measured apertures by the cross-sectional area, enabling consideration of both open and closed segments in the final calculation.

2.5.3. Aperture Field Evolution

The degree of $-\Delta e_m$ and asperity interaction for each σ' was determined through calculation of the contact area, R_c (%), between opposing fracture walls using a 2D projection of e_m as:

$$R_c = \frac{A_c}{A_t} \tag{8}$$

where A_c (m^2) is the contact between fracture faces and A_t (m^2) is the total fracture surface area. This approach meant that regions unoccupied by brine were segmented as R_c, which included all potential e_m's below the CT-scan resolution. The contribution of surface roughness to the evolving aperture field was investigated using the standard deviation, e^{σ}_m (μm), and mean of the aperture field, which enabled calculation of the relative roughness, e^{σ}_m/e_m (−), (Kling et al., 2017; Matsuki et al., 1999; Renshaw, 1995; Xie et al., 2015).

3. Results

3.1. Fracture Surface Roughness

Surface roughness is characterized in *x*- and *y*-directions for opposing top and bottom surfaces for samples *FR#1–FR#7* to quantify discrete roughness variations (Figure 3). *JRC*'s range between ∼2.5 (*FR#1*) and ∼7 (*FR#7*) (Figure 3b). Z_2 (Figure 3c) is empirically related to *JRC* (Equation 2); investigation into the top-*x*, bottom-*x*, top-*y*, and bottom-*y*-directions yield R^2 values of 0.99, 0.98, 0.98, and 0.99, respectively.

3.2. Fracture Permeability and Hydraulic Aperture

Figure 4a presents fracture permeability, k^f, evolution for *FR#1–FR#7* with incrementally increasing confining pressure, P_c, and thus effective stress, σ'. The resulting σ''s are directly related to each samples intrinsic permeability, illustrated most clearly by *FR#7*. k^f for all samples decreases exponentially with σ'. *FR#1–FR#6* (Figure 4b) display smaller k^f variation than seen in *FR#7* (Figure 4a). *FR#6* displays noticeably higher k^f (6.9×10^{-13}–1.8×10^{-13} m^2) in comparison to *FR#5*. *FR#7* spans the widest range of σ' (∼12.5 bar), corresponding to significantly higher k^f (2.2×10^{-12} m^2 at $\sigma' = 5.8$ bar; 5.3×10^{-13} m^2 at $\sigma' = 18.3$ bar) than observed in *FR#1–FR#6*. As *FR#7* displays a substantially greater k^f increase from *FR#6*, k^f (and e_h)

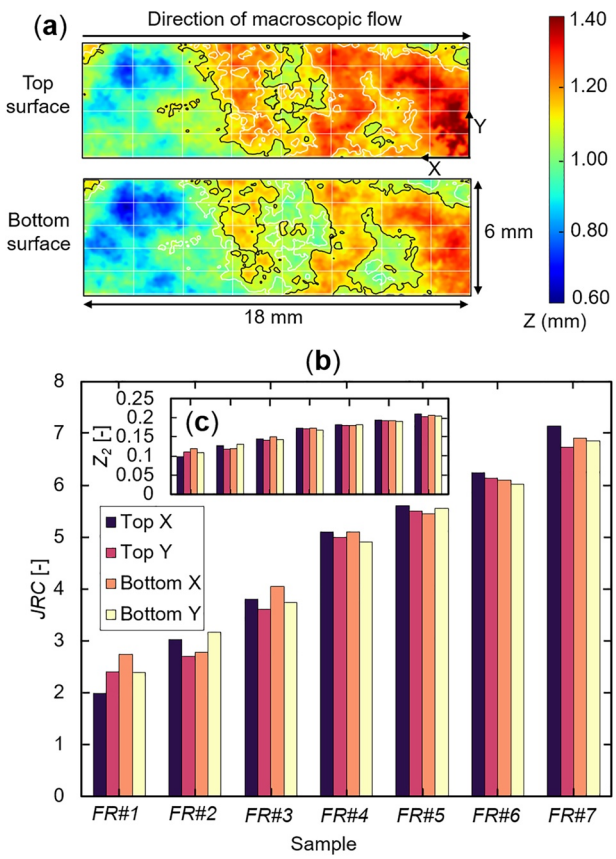

Figure 3. Fracture surface roughness in *x*- and *y*-directions for *FR#1–FR#7*. (a) Top and bottom 3D-printed fracture surfaces (from *FR#7*) denoting the direction of macroscopic flow and accompanying color map (*z*-dimension). Black contours represent the 1 mm height contour of that surface, with for reference in white the 1-mm contour of the opposing side of the fracture surface. Note that digital models of each fracture surface (*FR#1–FR#7*) are provided in Figure S2. *X*- and *y*-directions illustrate the sampling direction used in (b and c). (b) Mean joint roughness coefficient (*JRC*). (c) Mean Z_2.

measurements were conducted on the duplicate of *RF#7* (*FR#7_2*) during μ-CT aperture analysis (cf. Figure S8). Despite a higher flow rate, k^f response is consistent with that measured in the first instance.

Figure 4c illustrates the relationship between joint roughness coefficient, *JRC*, k^f, and σ'. Fractures with *JRC*'s between ~2.5 and 5.5 (*FR#1–FR#5*) show small k^f variation for each P_c increase. *JRC*'s > 6 (*FR#6–FR#7*) show significant k^f increases. For the first P_c step (11 bar), *FR#1* to *FR#5* shows only a 14% k^f increase. *FR#6* (*JRC* = ~6) shows a 40.8% k^f increase compared to *FR#5* for the first P_c step, representing a larger percentage increase than that observed for the entire range of *FR#1* to *FR#5*. *FR#7* shows a 219% k^f increase from *FR#6* for the first P_c step. The fracture with the highest *JRC* (~7, *FR#7*) corresponds to the highest k^f. k^f contrast between samples is consistently greater at lower P_c, exemplified by the decreasing horizontal distance between points with each P_c step (Figure 4c). For example, k^f for *FR#6* and *FR#7* decreases from 219% to 194% from the first to last P_c step, respectively.

We investigated the area available for advective flow by calculating hydraulic aperture, e_h, evolution with σ'. Aligning with k^f trends, decreasing e_h with increasing σ' is observed for all samples (Figure 4d). The minimum and maximum e_h values calculated are 1.41 μm (*FR#1* at 10. 5 bar σ') and 5.18 μm (*FR#7* at 5.8 bar σ'), respectively. Similar to k^f, e_h for *FR#7* shows consistently higher values than *FR#1–FR#6*. Even at the highest σ' imposed on *FR#7* (18.3 bar), the corresponding e_h (2.52 μm) is larger than that of all other samples across the full range of σ''s, barring the first P_c step for *FR#6* (2.87 μm at σ' = 4.8 bar).

3.3. (μ-CT) Imaged Mechanical Aperture

Figure 5 shows *FR#7_2*'s mechanical aperture, e_m, during four stepwise P_c (and resulting σ') increases (Table 1). Decreasing e_m is observed from 5 to 13.8 bar σ'. This is best shown visually by e_m maps (Figures 5a–5d), where decreasing thickness of larger aperture regions is accompanied by decreased connectivity of previously connected apertures (given the finite resolution of the images).

The mean (resolved) e_m ranges from 23.8 (5 bar σ') to 11.7 μm (13.8 bar σ'), representing a 50.8% decrease over 8.8 bar σ'. This corresponds to a 36.5% increase in contact area, R_c (Figure 5e), and a 78.4% increase in relative roughness, e_m^σ/e_m (Figure 5f). This results in a decreased area for advective flow, illustrated by a decreasing e_h (5.78–3.35 μm) (Figure 5g) and a 50.9% decrease in fracture volume, k^f_{vol} (Figure 5h). At 13.8 bar σ', the percentage of R_c and open (fluid-filled) aperture converge (48.2%). Aligning with these aperture changes, a 66.4% k^f decrease is observed from 5 to 13.8 bar σ', corresponding to a linear (R^2 = 0.98) decrease between e_m (12.1 μm decrease) and e_h (2.43 μm decrease) (Figure 5i). The (CL) e_h is up to 123.7% (at 9.2 bar σ') smaller than the measured (μ-CT) e_m.

Figure 6 illustrates e_m distribution with increasing σ' in the form of histograms (Figure 6a) and boxplots (Figure 6b). Increasing σ' prompts e_m decrease, demonstrated by a higher frequency of smaller apertures (Figure 6a), and decreases in standard deviation and whisker lengths (Figure 6b). Notably, all σ' steps display characteristic tailing toward larger e_m values, shown by a slight tendency toward positively (right) skewed distributions (Figure 6a).

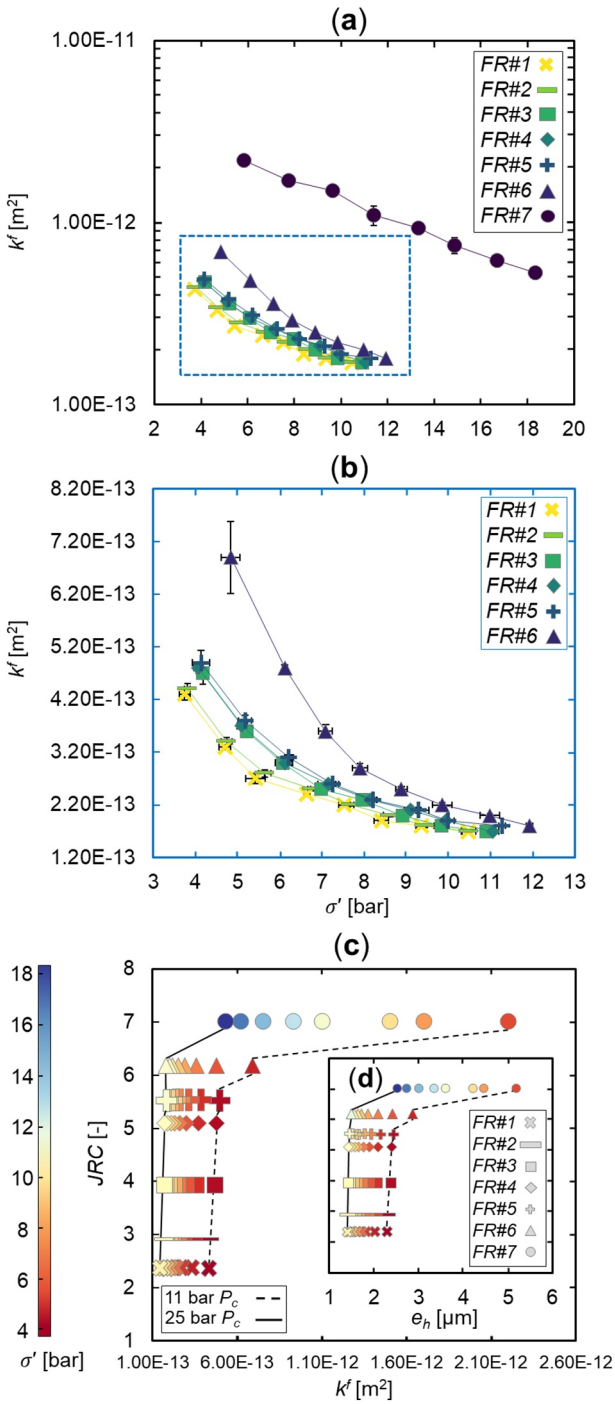

Figure 4. Measured fluid flow properties. (a) Fracture permeability (k^f) of *FR#1–FR#7* at eight incremental confining pressure (P_c) (and resulting effective stress (σ')) increases. (b) Enlarged view of k^f for *FR#1–FR#6* (boxed region in (a)). Error bars show ±1 standard deviation. (c) k^f, and (d) Hydraulic aperture (e_h) in relation to initially measured joint roughness coefficient (*JRC*), for each data point shown in (a). *JRC*'s represent the mean values in the direction of macroscopic flow (cf. Figure 3a). The first (lowest) and last (highest) P_c step are indicated by dashed and solid black lines, respectively. Note that all permeability values are reported in Table S3.

4. Discussion

4.1. 3DP Rock Proxies

4.1.1. Nature of 3DP Materials

We note that the chosen materials elastic properties (Table S2) differ from those observed in the majority of natural rocks. Accompanying uniform strength limitations, 3DP quality and consistency can be affected by expansion or shrinkage depending upon environmental surroundings, and irregularities or warped edges resulting from incorrect post-processing or improper build platform orientation (Bacher et al., 2015; Head & Vanorio, 2016; Ishutov et al., 2018). It is important to recognize these inherent limitations when drawing comparisons to natural rocks. However, through extensive analysis of available 3DP materials, Zhou and Zhu (2018) identified an SLA-based polymeric resin that best mimicked natural rock mechanical behavior, which has comparable elastic properties to the SLA-printed material used here. In the following, we discuss the applicability of using 3DP fractures as natural rock fracture proxies.

4.1.2. Applicability to Natural Fracture Roughness

Measured H values (Figure S6) compare favorably to those observed in natural faults and fractures ($H = 0.47$–0.84 ± 0.05) (e.g., Babadagli & Develi, 2003; Candela et al., 2009; Schmittbuhl et al., 1993). The *JRC* relation implemented (Equation 2) is relevant for the scale of samples (and roughness) analyzed here (mm-cm scale) and yields representative *JRC*'s for similar microscope derived datasets (Hale et al., 2019). Lithologically, the *JRC*'s investigated (~2.5–7) are representative of previously measured mudrocks (e.g., N. Barton & Choubey, 1977), fine-grained sandstones (e.g., Skurtveit et al., 2020) and granites (e.g., Tatone & Grasselli, 2010). It is therefore conceivable that learnings from this *JRC* range could be applied to scenarios where fractures play a predominant role, for example, caprock integrity for geological storage (e.g., mudrock) (Busch & Kampman, 2018), geothermal energy extraction (e.g., granite) (Martínez et al., 2014), or induced seismicity and unconventional gas extraction/enhanced oil recovery (e.g., mudrock and sandstone, respectively) (Davies et al., 2013; Grigoli et al., 2017).

4.1.3. Applicability to Natural Fracture Aperture

Using μ-CT data from *FR#7_2*, the maximum fracture aperture, $e_m^{\max}$ (μm), can be related to its length, following (Schlische et al., 1996; Vermilye & Scholz, 1995):

$$e_m^{\max} = \alpha \cdot L^n \tag{9}$$

where α represents a constant pertaining to the rock's mechanical properties, and n is a scaling exponent reported as being ~0.5 for opening mode fractures (Schultz et al., 2008). Applying this relationship yields $e_m^{\max}$ values compatible with our experimental data (within ~5% depending on mechanical properties). It is therefore reasonable that fracture properties obtained from these μ-CT images, such as R_c and aperture (and their impact on flow), can be upscaled into larger domains (cf. Ishibashi et al., 2015). It should, however, be acknowledged that e_m thresholds uncovered originate from a single rough fracture.

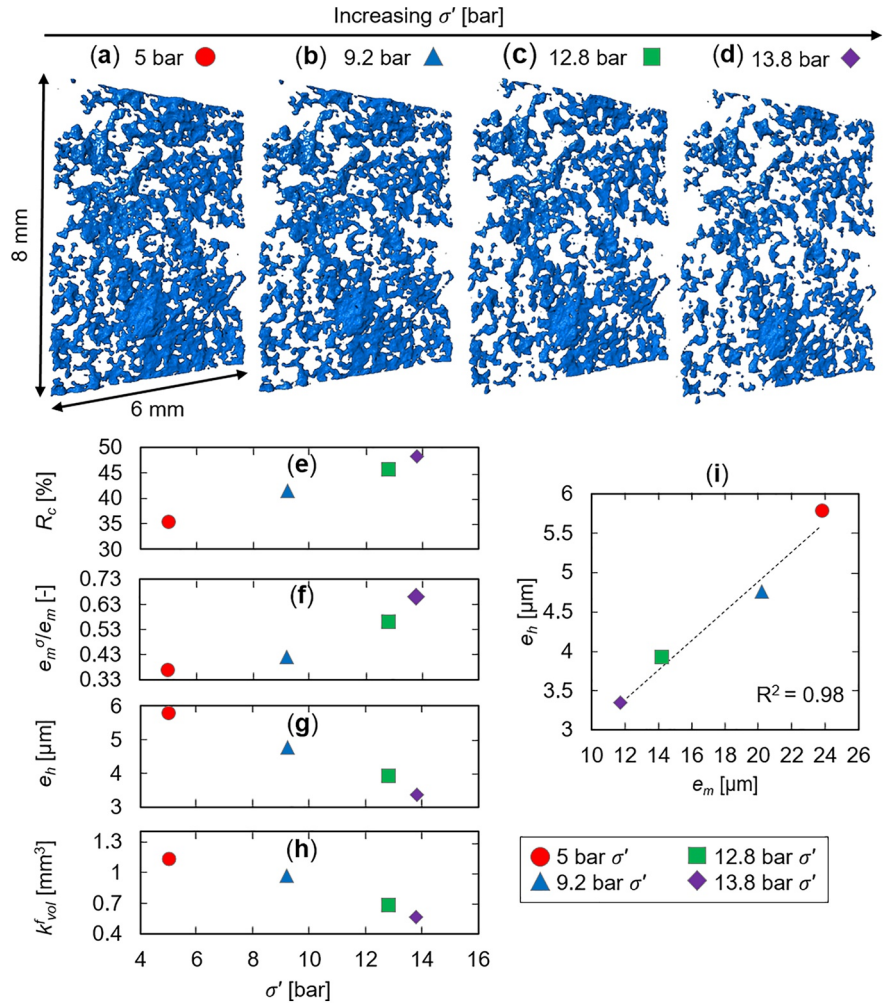

Figure 5. Fracture aperture evolution for *FR#7_2*. μ-CT maps of mechanical aperture (e_m) for four effective stress (σ') increases (a) 5, (b) 9.2, (c) 12.8, and (d) 13.8 bar. (e) Contact area (R_c), (f) Relative roughness (e_m^σ/e_m), (g) Hydraulic aperture (e_h), (h) Fracture pore volume $\left(k^f_{\text{vol}}\right)$, and (i) e_m versus e_h for each σ' increase shown in (a–d). The corresponding experimental parameters are detailed in Table 1. Note that all measured properties are provided in Table S4. μ-CT, micro-computed tomography.

4.1.4. Applicability to Natural Fracture Stiffness

Understanding fracture behavior during normal closure, particularly fracture stiffness, k_n (Pa.m) (i.e., $k_n = \Delta\sigma'/\Delta e_m$) (Jaeger et al., 2009), is key for knowledge transfer between synthetic and natural fractures. Among proposed empirical deformability models (e.g., Bandis et al., 1983; Goodman et al., 1968), the semi-logarithmic relation utilizes the stiffness characteristic, $\chi = \mathrm{d}k_n/\mathrm{d}\sigma'$ (mm^{-1}), to predict $-\Delta e_m$ resulting from $\Delta\sigma'$ in natural rock fractures (Evans et al., 1992):

$$-\Delta e_m = \frac{1}{\chi}\ln\left(\frac{\sigma'}{\sigma'_{\text{ref}}}\right) \tag{10}$$

where σ'_{ref} is an arbitrary reference value (i.e., $-\Delta e_m = 0$).

Applying Equation 10 to our stress-dependent e_m values (Figure 7a) indicates that despite material property differences, χ for *FR#7_2* falls within a range consistent with natural rock fractures (75.6 mm^{-1}) (Zangerl et al., 2008), highlighted by strong conformance to Equation 10 (Figure 7b, $R^2 = 0.9$). We, therefore, suggest that for the σ' range investigated here, stress-dependent fracture behavior observed in *FR#7_2* is a reasonable approximation of natural fracture $-\Delta e_m$ behavior. With this, we compare stress-dependent permeability response with widely used empirical models for natural fractures in Section 4.4.

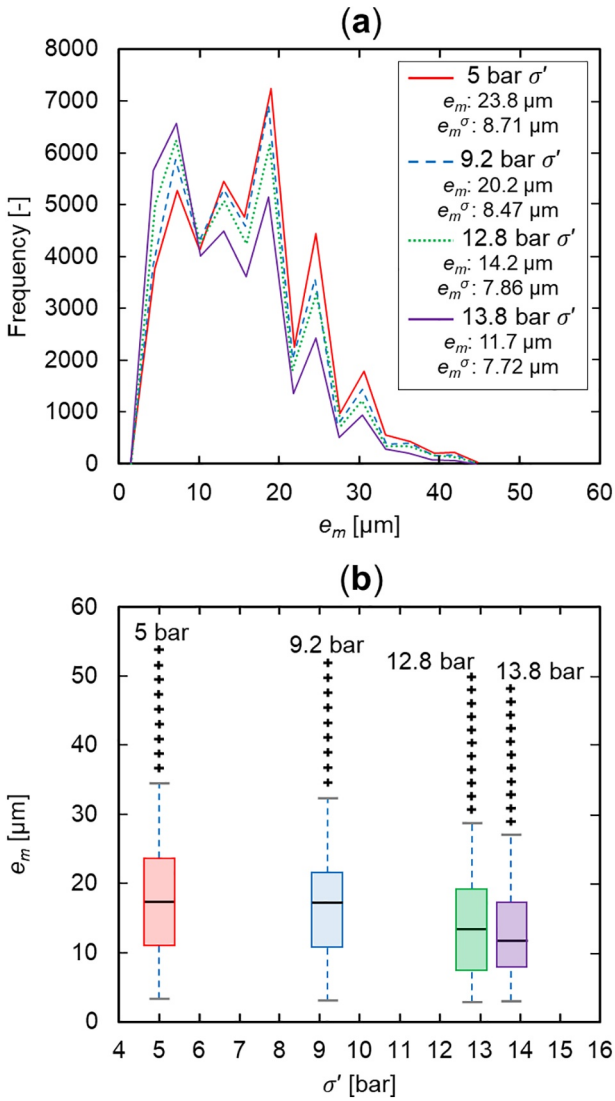

Figure 6. *FR#7_2* aperture distributions. (a) Mechanical aperture (e_m) frequency distributions for each effective stress (σ') increase shown in Figure 5. (b) Boxplots for each σ' increase, with the central black line representing the median, and the box and whiskers denoting the interquartile, and the 5th to 95th percentile ranges, respectively.

4.2. Effect of Fracture Surface Roughness on Permeability

In this study, fractures with higher roughness exhibit higher k^f (Figure 4). Conspicuously, higher roughness corresponds to larger e_h's (Figures 4c and 4d), increasing the area available for advective flow. In the literature, k^f has been reported to decrease with roughness on account of higher energy dissipation caused by protruding asperities (e.g., Brown, 1987; Crandall, Bromhal, & Karpyn, 2010; Moreno et al., 1988; Qian et al., 2011; Y. W. Tsang, 1984; J. B. Walsh & Brace, 1984; J. S. Y. Wang et al., 1988; Zambrano et al., 2019). Contrasting this, fractures with a given amount of surface mismatch (e.g., shear) indicate k^f increases with roughness due to the creation of larger voids which enhance flow (Fang et al., 2018; N. Huang et al., 2018; Zambrano et al., 2019). From our results, we conclude that higher k^f is the result of increasingly larger apertures (*FR#1*, maximum e_h = 2.28 μm; *FR#7*, maximum e_h = 5.18 μm), as opposed to concluding that higher roughness directly corresponds to higher k^f.

Fractures with *JRC*'s < 5.5 (*FR#1–FR#5*) display comparably smaller k^f changes across the full P_c range than *JRC*'s > 6 (*FR#6* and *FR#7*; Figure 4). *JRC* exerts a greater influence on k^f at lower σ', illustrated by the largest k^f variations corresponding to the lowest σ' (Figures 4a and 4b). This is evident even in fractures with similar k^f response (*FR#1–FR#5*), with a 13% difference at 11 bar P_c, compared to 5.7% at 25 bar P_c. Such behavior highlights the importance of roughness on k^f at lower σ' (when e_h is > 2 μm), consistent with previously reported flow behavior (Y. Chen et al., 2019).

Near linear relationships (R^2 = 0.79–0.98) between *JRC* and k^f are seen in *FR#1–FR#5*, with this trend becoming exponential when *JRC* > 6 (*FR#6–FR#7*; Figure 4). Considering laminar flow, as investigated here, numerical approaches suggest a variety of *JRC*–k^f correlations, from near-linear decreases (e.g., Crandall, Bromhal, & Karpyn, 2010; Yin et al., 2019) to near-linear increases (e.g., Rasouli & Hosseinian, 2011), depending on aperture size and asperity arrangement. We find linear *JRC*–k^f relations to be valid only in smoother fractures (*JRC* < 5.5), suggesting that flow properties not captured in these models may exist. For the roughness distributions investigated here, a transition to a more connected aperture geometry may occur between *JRC* = 6–7, leading to this nonlinear k^f response. Additionally, fracture wall roughness has been shown to strongly influence the severity of flow channeling (e.g., Méheust & Schmittbuhl, 2001), which could suggest that this roughness (and e_h) increase, and resulting aperture structure alteration, enhances the propensity for strong flow-enhancing channels to arise. However, such a finding primarily supports the notion that *JRC* alone is incapable of predicting k^f, and requires more detailed investigation into aperture structure (Rezaei Niya & Selvadurai, 2019).

4.3. Fracture Aperture

In the following, we discuss measured fracture properties obtained via concurrent fluid flow–μ-CT analysis of *FR#7_2*, with specific focus on the interplay between roughness, R_c, and aperture, and their contribution to k^f.

4.3.1. Aperture Field Evolution With Effective Stress

e_m (maximum, median and mean) decreases with σ' (Figure 6), consistent with aforementioned laboratory-based studies. Such findings are intuitive, considering opposing fracture walls subjected to increasing σ' will inevitably reduce void space. Fracture voids exhibit crack-like morphology, contrasting the more oval or

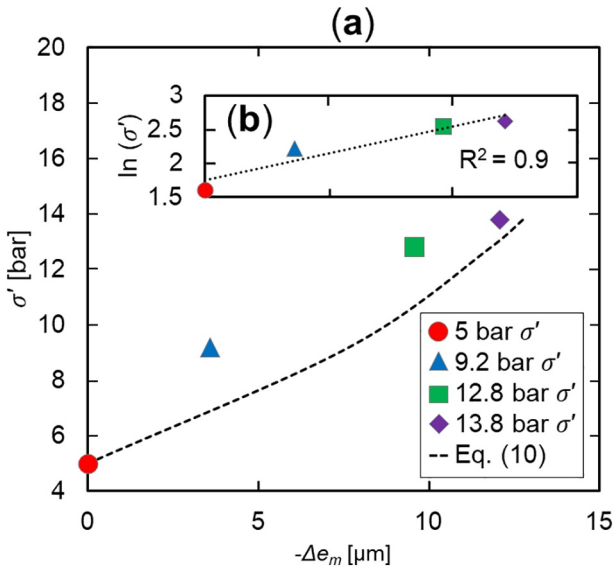

Figure 7. Fracture aperture evolution with effective stress. (a) Fitting of the semi-logarithmic closure law (Equation 10) to stress-induced (σ') fracture normal closure ($-\Delta e_m$) data shown in Figure 5. (b) Linear regression analysis of the logarithm (ln) of σ', highlighting the conformity between experimental data and model prediction.

triangular pore-morphology seen in porous media (Council, 1996). This characteristic geometry, coupled with the fact that these samples are unconsolidated, means that fractures display high stress sensitivity.

e_m distributions narrow with increasing σ', illustrated by positive skewness (Figure 6a), consistent with previously measured rough fracture aperture distributions (Gentier et al., 1997; Pruess & Tsang, 1990; Sharifzadeh et al., 2008; Tatone & Grasselli, 2012; Y. W. Tsang & Tsang, 1990). $-\Delta e_m$ with σ' has also been shown to be heterogeneous, with skewness increasing in prevalence (i.e., longer tail) (Javanmard et al., 2021; Kang et al., 2016; Muralidharan et al., 2004; Unger & Mase, 1993; R. Walsh et al., 2008), aligning with distributions seen here, albeit subtly. The lower cut-offs observed for each σ' are likely controlled by voxel size.

4.3.2. Evolving Aperture Structure and Its Effect on Flow Properties

For the σ' range investigated, R_c varies from 35.3% to 48.2%, which falls within the range reported in previous studies for natural rock fractures (~15%–60%) (Ishibashi et al., 2015; Montemagno & Pyrak-Nolte, 1999; Pyrak-Nolte et al., 1987; Skurtveit et al., 2020; Y. W. Tsang & Witherspoon, 1981; Watanabe et al., 2008). Increasing $-\Delta e_m$ results in increased R_c, which weakens the CL's (Equation 1) validity, and leads to the disparity observed between e_m and e_h. The (CL) e_h is consistently smaller than the (μ-CT) e_m (Figure 5i), aligning with studies suggesting these apertures cannot be equated (Olsson & Barton, 2001; Vogler et al., 2016). e_h reduction (42%) is smaller than that of e_m (50.8%) from 5 to 13.8 bar σ' due to larger apertures being forced to close, while, the void configuration between stressed asperities enables preferential flow channels to exist (Kang et al., 2016; Nemoto et al., 2009), yielding comparably smaller e_h changes.

Although R_c increases with σ', consistent with previous studies (B. Li et al., 2008), the measure of tortuosity given by e_h/e_m increases from 0.24 (5 bar σ') to 0.28 (9.2 bar σ'), with lower values indicating higher tortuosity (Ishibashi et al., 2018; Matsuki et al., 2006). This suggests that overall (from 5 to 13.8 bar σ'), increasing R_c does not correspond to increasing tortuosity, however, at lower σ' (from 5 to 9.2 bar σ'), tortuosity increases, supporting the notion that increased R_c yields higher tortuosity (Muralidharan et al., 2004; Y. W. Tsang, 1984; von Planta et al., 2019). This could suggest that the preferential flow channels, which facilitate the majority of the flow and require higher stresses to close (Pyrak-Nolte & Nolte, 2016; Rasmuson & Neretnieks, 1986), are not significantly impacted by this R_c increase. However, increasing tortuosity is observed from 5 (0.1) to 13.8 (0.07) bar σ' when consideration of $e_m^{\max}$ ($e_h/e_m^{\max}$) is given. It is also the case that despite a certain correlation between R_c and tortuosity, this relationship alone cannot adequately capture aperture heterogeneity (in relation to tortuosity), as R_c only accounts for a portion of the fracture surface (Rong et al., 2020). Tortuosity is therefore also dependent on the evolution of overall surface and resulting aperture structure roughness, which is observed to increase ($e_m^{\sigma}/e_m = 0.37$ to 0.66) with σ', with e_m decreasing more rapidly than e_m^{σ}, consistent with previous studies (Javanmard et al., 2021). Although it is evident that tortuosity plays a significant role in *FR#7_2*'s k^f decrease, and, by proxy, the k^f response of *FR#1–FR#6*, identifying which tortuosity-contributing parameter primarily influences k^f is key.

4.4. Stress-Dependent Fracture Permeability

k^f is governed by aperture, e_m^{σ}/e_m, and R_c; all of which are stress-dependent (Zimmerman & Bodvarsson, 1996). In the following, we compare widely adopted empirical models to experimental data obtained from *FR#7_2* (Figure 8, gray line with symbols) to determine the relative contributions of each on stress-dependent k^f.

Applying R_c data (Figure 5e) to account for tortuosity ($1–2R_c$) coupled with e_m^{σ}/e_m, via (Zimmerman & Bodvarsson, 1996) (Figure 8, dashed red line):

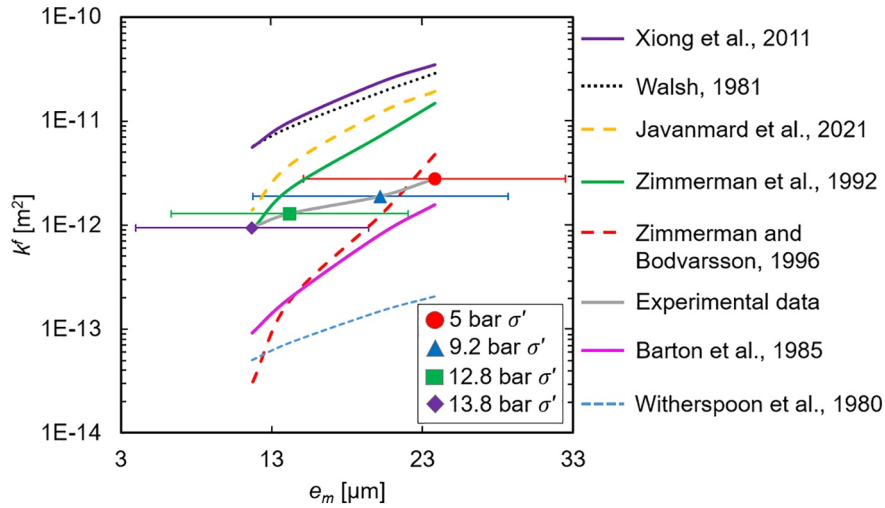

Figure 8. Aperture-permeability relationship for *FR#7_2*. (a) Empirical model predictions of stress-dependent fracture permeability (k^f) evolution for natural rock fractures, accompanied by experimental mechanical aperture (e_m) data from this study. e_m error bars represent ±1 standard deviation. k^f error bars are too small to be legible.

$$e_h = \frac{e_m}{\sqrt[3]{1 - 1.5\left(\frac{e_m^\sigma}{e_m}\right)^2}}\left(1 - 2R_c\right) \tag{11}$$

yields reasonable k^f estimations at lower σ' (within 42% at 9.2 bar σ'), but large underestimations at higher σ'. The inadequacy of e_m^σ/e_m alone as a k^f predictor is affirmed by the relation of X. Xiong et al. (2011) (Figure 8, solid purple line):

$$e_h = e_m\sqrt[3]{1 - \frac{e_m^\sigma}{e_m}} \tag{12}$$

Similar overestimations are observed for other empirical models utilizing e_m^σ/e_m (e.g., N. Barton & de Quadros, 1997; Brown, 1987; Kling et al., 2017; Matsuki et al., 1999; Renshaw, 1995; Zimmerman et al., 1991). Other studies have incorporated e_m^σ/e_m coupled with the concept of a no-flow fraction, as it has been shown that flow is not only diminished at specific contacting asperities (i.e., R_c alone), but also in the surrounding void area (B. Li et al., 2008; Yeo, 2001). k^f estimation from this method (Javanmard et al., 2021) (Figure 8, dashed yellow line):

$$k^f = \frac{e_m^2}{12\left(1 + \left(\frac{e_m^\sigma}{e_m}\right)^2\right)}\left(0.6188 - 0.8266\frac{e_m^\sigma}{e_m}\right)^{2/3} \tag{13}$$

yields reasonable k^f estimation at the highest σ' (within 39%). Nevertheless, insufficient k^f predictions given by these relations imply surface roughness should be considered to better predict experimental k^f, particularly at lower σ'.

Modifying the CL (Equation 1) to account for the degree to which surface roughness causes deviations from the parallel-plate model can be captured via a friction factor, f (−) (Zambrano et al., 2019):

$$f = \frac{S_z}{2e_h} \tag{14}$$

where S_z is the difference between the highest peak and lowest pit of the physical surface roughness. Using f computed at initial loading (Table S5), Equation 1 reformulates, giving a modified cubic law (MCL) (Witherspoon et al., 1980):

$$Q = -\frac{1}{f}\frac{we_m^3}{12\eta}\Delta P \tag{15}$$

Applying Equation 15 (Figure 8, blue dashed line) to our experimental data results in lower k^f due to higher friction. Increasing σ' amplifies the impact of roughness (and tortuosity) and yields larger f values, consistent with studies in rough fractures (e.g., Huo & Benson, 2015; Zhang & Nemcik, 2013). This roughness amplification is mirrored by the linear trend ($R^2 = 0.97$) of e_m^σ/e_m (5 bar $\sigma' = 0.37$, 13.8 bar $\sigma' = 0.66$). Considering a scenario where k^f decrease is entirely attributable to aperture closure, Equation 15 would reduce to Equation 1 and match experimental data, which is not the case.

Relating e_h and e_m using the measured JRC, via (C. A. Barton et al., 1985) (Figure 8, solid pink line):

$$e_h = \frac{e_m^2}{JRC^{2.5}} \tag{16}$$

provides a reasonable fit to experimental data for the first two σ''s (within 55% at 5 bar σ'), however, decreases in effectiveness with σ', suggesting roughness plays a more significant role in governing k^f at lower σ' (larger e_m).

To exclusively identify the contribution of R_c to k^f, we implement R_c coupled with the assumption of circular contact areas, following the conceptual expression (J. B. Walsh, 1981):

$$e_h^3 = e_m^3\frac{\left(1 - R_c\right)}{\left(1 + R_c\right)} \tag{17}$$

This model (Figure 8, dotted black line) fails to predict k^f by ~one order of magnitude, due to a combination of simplified R_c and decreased applicability of this relationship when $R_c > 25\%$ (Zimmerman et al., 1992). Modifying Equation 17 to represent more realistic cases is achieved through assigning elliptical contact regions, via (Zimmerman et al., 1992):

$$e_h^3 = e_m^3\frac{\left(1 - \beta R_c\right)}{\left(1 + \beta R_c\right)} \tag{18}$$

where β [−] is related to the aspect ratio of the ellipse, b [−], given by:

$$\beta = \frac{\left(1 + b\right)^2}{4b} \tag{19}$$

and where b is estimated from fitting to experimental data ($b = 0.17$). This relation (Figure 8, solid green line) predicts consistently lower k^f than the J. B. Walsh (1981) model as β increases monotonically through ellipse elongation (cf. Zimmerman et al., 1992). Both models, reliant on R_c values obtained at this CT-scanning resolution, are incapable of fully replicating experimental k^f.

Of the empirical relations applied, tortuosity (Equation 11) and surface roughness (Equation 16) are the best k^f predictors at lower σ' ($e_m = >\sim 20$ μm, $e_m^\sigma/e_m = <\sim 0.42$). With increasing σ' ($e_m = <\sim 20$ μm, $e_m^\sigma/e_m = >\sim 0.42$), both the no-flow fraction (Equation 13) and R_c (Equation 18) relationships increase in predictivity with $-\Delta e_m$, with the Zimmerman et al. (1992) model within 4% of experimental k^f at 13.8 bar σ'. Unsatisfactory predictions from the MCL, C. A. Barton et al. (1985) and J. B. Walsh (1981) relations attest that for smaller aperture fractures ($e_m = <\sim 20$ μm, $e_m^\sigma/e_m = >\sim 0.42$), both surface roughness and simplified R_c are inadequate for predicting stress-dependent k^f.

4.5. Implications for the Natural Rock Fracture Domain

4.5.1. 3D Printing Advancements

Again, we note that natural fractures may display larger magnitudes of heterogeneity, particularly in terms of material properties. Therefore, despite possessing roughness, R_c, and aperture distributions analogous to natural fractures, the heterogeneous nature of natural fractures means that these 3DP fractures are not perfect analogs and different hydromechanical responses cannot be discounted. However, provided proper acknowledgment and understanding of the current limitations are afforded (Section 4.1.1); we demonstrate that 3DP fractures using this material produces reasonable approximations of natural fractures for the σ''s investigated here (Sections 4.1.2–4.1.4). 3DP offers the control to investigate complex geometries repeatedly, as demonstrated here (as low as 1.6% difference in roughness), a utility that is simply unattainable in natural rocks. This systematic parametrization of fracture geometry (and its impact on flow) is the nexus between laboratory studies and numerical models, while also furthering the discussion on the applicability of 3DP materials as natural fracture proxies.

4.5.2. Stress-Permeability Relationships

Natural rock k^f can be impacted by asperity destruction and gouge formation during loading and/or shearing (Ishibashi et al., 2018; Yeo et al., 1998). Such deformation processes have been observed in polymeric fractures during shearing despite comparably higher asperity ductility (Ishibashi et al., 2020). Here, samples are not sheared (cf. Text S7) or subjected to cyclic loading (which has also been shown to impact k^f [G. Wang, Mitchell, et al., 2016]). Visual inspection of all fractures post-experiment indicate no discernible surface damage, which suggests that said mechanisms do not influence stress-permeability relationships for the σ''s, material and timeframes investigated here. Future experiments wishing to subject polymeric 3DP fractures to higher (normal or shear) stresses for prolonged periods should consider the influence of these mechanisms, which may differ in terms of pervasiveness and severity compared to natural rocks with varying mechanical properties.

4.5.3. Extending Roughness Analysis to Natural Systems

In default of subsurface observations, extending laboratory-scale roughness studies and subsequent effects on flow relies on empirical relations. For example, it has been demonstrated that the scale-independency of R_c provides unique opportunities to predict aperture distributions from the laboratory to the field-scale (cf. Ishibashi et al., 2015). Despite the challenges associated with measuring reliable aperture structures, for example, from outcropping barren fractures altered by exhumation and weathering, direct (2D μm–cm-scale) aperture measurements from outcrop and core can be acquired via scanline sampling techniques (e.g., Casini et al., 2011; Lepillier et al., 2020; Watkins et al., 2015) and vein measurements (e.g., Gale et al., 2014; Ukar et al., 2019). R_c estimation from these methods, coupled with aforementioned empirical relations, provides a promising approach for predicting k^f in the absence of direct measurements (i.e., flow tests). Additionally and conversely, the presence of flow tests could provide opportunities to verify such predictions.

5. Conclusions

In this systematic study, fluid flow experiments were performed to ascertain permeability contrasts between seven 3D-printed fractures with different surface roughness distributions akin to natural fractures. Stress-dependent aperture evolution in the roughest fracture was investigated using laboratory-based μ-CT. From this study, we conclude that:

1. Polymeric 3D-printed fractures provide the opportunity to systematically scrutinize rough fracture properties, which can be used to improve our understanding of natural subsurface fracture flow
2. The fractures with higher roughness have larger hydraulic apertures, corresponding to increasing fracture permeability with *JRC*. This is coupled with exponentially decreasing fracture permeability with increasing effective stress
3. At the lowest effective stresses, the fractures with lower *JRC*'s (∼2.5–∼5.5) display relatively small fracture permeability (14% increase) and hydraulic aperture (7% increase) variations. However, a *JRC* of ∼6 compared to ∼5.5 shows a fracture permeability increase of up to 41%, larger than that observed between

all previous fractures ($JRC = \sim 2.5$ to ~ 5.5) combined. A fracture with a JRC of ~ 7 shows an increase of up to 219% in fracture permeability compared to a fracture with a JRC of ~ 6. For the experimental method documented in this study, and for this specific sample set, we find that when $JRC > 6$ fracture permeability is not linearly related but rather exponentially. The validity of this behavior in relation to other 3D-printed or natural fractures requires further research but nonetheless provides unique insight into our understanding of fluid flow in rough fractures

4. μ-CT imaging of the roughest fracture shows that the cubic law hydraulic aperture is consistently smaller than the (μ-CT) mechanical aperture. With increasing effective stress (5–13.8 bar), fracture contact area increases (35%–48%), which yields a relatively rougher (from 0.37 to 0.66) fracture aperture distribution that becomes increasingly skewed as a result
5. We considered the impact of relative roughness, initial surface roughness, tortuosity, no-flow fraction, and contact area on fracture permeability predictivity via application of previously published empirical aperture-permeability relations to our μ-CT experimental data. Our experimental findings indicate that knowledge of contact area is more beneficial to predict fracture permeability than initial surface roughness at higher effective stress, which is, consequently, relevant to most natural subsurface fracture systems, which are synonymous with high effective stresses

Conflict of Interest

The authors have no competing interest to declare.

Data Availability Statement

The experimental micro-CT data are publically available via the digital rocks portal, listed as "Stress-Dependent Fluid Flow in a 3D-Printed Rough Fracture" (https://doi.org/10.17612/xgv3-1k27).

Acknowledgments
The authors greatly acknowledge Thomas McGravie for printing samples and for valuable discussions throughout each phase of 3D printing. The authors further thank Shell Global Solutions International B. V. for access to the digital optical microscope at Shell Technology Centre Amsterdam and UGCT (the center for X-ray tomography at Ghent University). The authors thank Shell Global Solutions International B. V. for supporting publication of this article. Tom Bultreys is a postdoctoral fellow of the Research Foundation-Flanders (FWO) and acknowledges its support under grant 12X0919N. Arjen Mascini acknowledges support from Research Foundation Flanders (FWO, project G051418N). Part of this project has been subsidized through the ERANET Cofund ACT (Project no. 271497), the European Commission, the Research Council of Norway, the Rijksdienst voor Ondernemend Nederland, the Bundesministerium für Wirtschaft und Energie, and the Department of Business, Energy & Industrial Strategy, UK. This work is also part of a project that has received funding by the European Union's Horizon 2020 research and innovation programme, under grant agreement number 764531. We thank the three anonymous reviewers and associate editor for detailed feedback on an earlier version of this manuscript, which significantly improved the overall quality.

References

Adler, P. M., Thovert, J. F., & Mourzenko, V. V. (2012). *Fractured porous media*. Oxford: OUP.

Ai-Yaarubi, A. H., Pain, C. C., Grattoni, C. A., & Zimmerman, R. W. (2005). Navier-Stokes simulations of fluid flow through a rock fracture. In B. Faybishenko, P. A. Witherspoon, & J. Gale (Eds.), *Dynamics of fluids and transport in fractured rock* (pp. 55–64). Geophysical Monograph Series. https://doi.org/10.1029/162GM07

Austad, T., Shariatpanahi, S. F., Strand, S., Black, C. J. J., & Webb, K. J. (2012). Conditions for a low-salinity enhanced oil recovery (EOR) effect in carbonate oil reservoirs. *Energy & Fuels*, *26*(1), 569–575. https://doi.org/10.1021/ef201435g

Babadagli, T., & Develi, K. (2003). Fractal characteristics of rocks fractured under tension. *Theoretical and Applied Fracture Mechanics*, *39*(1), 73–88. https://doi.org/10.1016/s0167-8442(02)00139-8

Bacher, M., Schwen, A., & Koestel, J. (2015). Three-dimensional printing of macropore networks of an undisturbed soil sample. *Vadose Zone Journal*, *14*(2). https://doi.org/10.2136/vzj2014.08.0111

Bandis, S. C., Lumsden, A. C., & Barton, N. R. (1983). Fundamentals of rock joint deformation. *International Journal of Rock Mechanics and Mining Science & Geomechanics Abstracts*, *20*(6), 249–268. https://doi.org/10.1016/0148-9062(83)90595-8

Barbosa, K., Chalaturnyk, R., Bonfils, B., Esterle, J., & Chen, Z. (2020). Testing impact load cell calculations of material fracture toughness and strength using 3D-printed sandstone. *Geotechnical & Geological Engineering*, *38*(2), 1065–1096. https://doi.org/10.1007/s10706-019-01073-y

Barton, C. A., Zoback, M. D., & Moos, D. (1995). Fluid flow along potentially active faults in crystalline rock. *Geology*, *23*(8), 683–686. https://doi.org/10.1130/0091-7613(1995)023<0683:ffapaf>2.3.co;2

Barton, N., Bandis, S., & Bakhtar, K. (1985). Strength, deformation and conductivity coupling of rock joints. *International Journal of Rock Mechanics and Mining Science & Geomechanics Abstracts*, *22*(3), 121–140. https://doi.org/10.1016/0148-9062(85)93227-9

Barton, N., & Choubey, V. (1977). The shear strength of rock joints in theory and practice. *Rock Mechanics*, *10*, 1–54. https://doi.org/10.1007/bf01261801

Barton, N., & de Quadros, E. F. (1997). Joint aperture and roughness in the prediction of flow and groutability of rock masses. *International Journal of Rock Mechanics and Mining Sciences*, *34*(3–4), 252.e1–252.e14. https://doi.org/10.1016/s1365-1609(97)00081-6

Berkowitz, B. (2002). Characterizing flow and transport in fractured geological media: A review. *Advances in Water Resources*, *25*(8–12), 861–884. https://doi.org/10.1016/s0309-1708(02)00042-8

Bisdom, K., Bertotti, G., & Nick, H. M. (2016). The impact of different aperture distribution models and critical stress criteria on equivalent permeability in fractured rocks. *Journal of Geophysical Research: Solid Earth*, *121*(5), 4045–4063. https://doi.org/10.1002/2015jb012657

Boutt, D. F., Grasselli, G., Fredrich, J. T., Cook, B. K., & Williams, J. R. (2006). Trapping zones: The effect of fracture roughness on the directional anisotropy of fluid flow and colloid transport in a single fracture. *Geophysical Research Letters*, *33*(21). https://doi.org/10.1029/2006gl027275

Brace, W. F. (1980). Permeability of crystalline and argillaceous rocks. *International Journal of Rock Mechanics and Mining Science & Geomechanics Abstracts*, *17*(5), 241–251. https://doi.org/10.1016/0148-9062(80)90807-4

Briggs, S., Karney, B. W., & Sleep, B. E. (2017). Numerical modeling of the effects of roughness on flow and eddy formation in fractures. *Journal of Rock Mechanics and Geotechnical Engineering*, *9*(1), 105–115. https://doi.org/10.1016/j.jrmge.2016.08.004

Brown, S. R. (1987). Fluid flow through rock joints: The effect of surface roughness. *Journal of Geophysical Research*, *92*(B2), 1337–1347. https://doi.org/10.1029/jb092ib02p01337

Brown, S. R. (1995). Simple mathematical model of a rough fracture. *Journal of Geophysical Research*, *100*(B4), 5941–5952. https://doi.org/10.1029/94jb03262

Brown, S. R., Caprihan, A., & Hardy, R. (1998). Experimental observation of fluid flow channels in a single fracture. *Journal of Geophysical Research*, *103*(B3), 5125–5132. https://doi.org/10.1029/97jb03542

Brown, S. R., & Scholz, C. H. (1985a). Broad bandwidth study of the topography of natural rock surfaces. *Journal of Geophysical Research*, *90*(B14), 2575–2582. https://doi.org/10.1029/jb090ib14p12575

Brown, S. R., & Scholz, C. H. (1985b). Closure of random elastic surfaces in contact. *Journal of Geophysical Research*, *90*(NB7), 5531–5545. https://doi.org/10.1029/jb090ib07p05531

Brush, D. J., & Thomson, N. R. (2003). Fluid flow in synthetic rough-walled fractures: Navier-stokes, stokes, and local cubic law simulations. *Water Resources Research*, *39*(4). https://doi.org/10.1029/2002wr001346

Buades, A., Coll, B., & Morel, J.-M. (2005). A non-local algorithm for image denoising (Vol. 2, pp. 60–65). Proceedings of IEEE Computer Society Conference on Computer Vision and Pattern Recognition. https://doi.org/10.1109/CVPR.2005.38

Buades, A., Coll, B., & Morel, J.-M. (2008). Nonlocal image and movie denoising. *International Journal of Computer Vision*, *76*(2), 123–139. https://doi.org/10.1007/s11263-007-0052-1

Bultreys, T., Boone, M. A., Boone, M. N., De Schryver, T., Masschaele, B., Van Hoorebeke, L., & Cnudde, V. (2016). Fast laboratory-based micro-computed tomography for pore-scale research: Illustrative experiments and perspectives on the future. *Advances in Water Resources*, *95*, 341–351. https://doi.org/10.1016/j.advwatres.2015.05.012

Busch, A., & Kampman, N. (2018). Migration and leakage of CO_2 from deep geological storage sites. In S. Vialle, J. Ajo-Franklin, & J. W. Carey (Eds.), *Geological carbon storage* (pp. 285–302). https://doi.org/10.1002/9781119118657.ch14

Candela, T., Renard, F., Bouchon, M., Brouste, A., Marsan, D., Schmittbuhl, J., & Voisin, C. (2009). Characterization of fault roughness at various scales: Implications of three-dimensional high resolution topography measurements. *Pure and Applied Geophysics*, *166*(10–11), 1817–1851. https://doi.org/10.1007/s00024-009-0521-2

Candela, T., Renard, F., Klinger, Y., Mair, K., Schmittbuhl, J., & Brodsky, E. E. (2012). Roughness of fault surfaces over nine decades of length scales. *Journal of Geophysical Research*, *117*. https://doi.org/10.1029/2011jb009041

Casini, G., Gillespie, P. A., Vergés, J., Romaire, I., Fernández, N., Casciello, E., et al. (2011). Sub-seismic fractures in foreland fold and thrust belts: Insight from the Lurestan Province, Zagros Mountains, Iran. *Petroleum Geoscience*, *17*(3), 263–282. https://doi.org/10.1144/1354-079310-043

Chen, Y., Lian, H., Liang, W., Yang, J., Nguyen, V. P., & Bordas, S. P. A. (2019). The influence of fracture geometry variation on non-Darcy flow in fractures under confining stresses. *International Journal of Rock Mechanics and Mining Sciences*, *113*, 59–71. https://doi.org/10.1016/j.ijrmms.2018.11.017

Chen, Z., Narayan, S. P., Yang, Z., & Rahman, S. S. (2000). An experimental investigation of hydraulic behaviour of fractures and joints in granitic rock. *International Journal of Rock Mechanics and Mining Sciences*, *37*(7), 1061–1071. https://doi.org/10.1016/s1365-1609(00)00039-3

Chen, Z., Qian, J., Zhan, H., Zhou, Z., Wang, J., & Tan, Y. (2017). Effect of roughness on water flow through a synthetic single rough fracture. *Environmental Earth Sciences*, *76*(4), 186. https://doi.org/10.1007/s12665-017-6470-7

Council, N. R. (1996). *Rock fractures and fluid flow: Contemporary understanding and applications* (p. 568). Washington, DC: The National Academies Press. https://doi.org/10.17226/2309

Crandall, D., Ahmadi, G., & Smith, D. H. (2010). Computational modeling of fluid flow through a fracture in permeable rock. *Transport in Porous Media*, *84*(2), 493–510. https://doi.org/10.1007/s11242-009-9516-9

Crandall, D., Bromhal, G., & Karpyn, Z. T. (2010). Numerical simulations examining the relationship between wall-roughness and fluid flow in rock fractures. *International Journal of Rock Mechanics and Mining Sciences*, *47*(5), 784–796. https://doi.org/10.1016/j.ijrmms.2010.03.015

Darcy, H. (1856). *Les fountaines publiques de la ville de Dijon*. Paris: Victor Dalmont.

Davies, R., Foulger, G., Bindley, A., & Styles, P. (2013). Induced seismicity and hydraulic fracturing for the recovery of hydrocarbons. *Marine and Petroleum Geology*, *45*, 171–185. https://doi.org/10.1016/j.marpetgeo.2013.03.016

de Dreuzy, J. R., Meheust, Y., & Pichot, G. (2012). Influence of fracture scale heterogeneity on the flow properties of three-dimensional discrete fracture networks (DFN). *Journal of Geophysical Research*, *117*. https://doi.org/10.1029/2012jb009461

Dou, Z., Sleep, B., Zhan, H., Zhou, Z., & Wang, J. (2019). Multiscale roughness influence on conservative solute transport in self-affine fractures. *International Journal of Heat and Mass Transfer*, *133*, 606–618. https://doi.org/10.1016/j.ijheatmasstransfer.2018.12.141

Durham, W. B., & Bonner, B. P. (1994). Self-propping and fluid flow in slightly offset joints at high effective pressures. *Journal of Geophysical Research*, *99*(B5), 9391–9399. https://doi.org/10.1029/94jb00242

Esaki, T., Du, S., Mitani, Y., Ikusada, K., & Jing, L. (1999). Development of a shear-flow test apparatus and determination of coupled properties for a single rock joint. *International Journal of Rock Mechanics and Mining Sciences*, *36*(5), 641–650. https://doi.org/10.1016/s0148-9062(99)00044-3

Evans, K. F., Kohl, T., Rybach, L., & Hopkirk, R. J. (1992). The effects of fracture normal compliance on the long term circulation behaviour of a hot dry rock reservoir: A parameter study using the new fully-coupled code fracture. *Geothermal Resources Council Transactions*, *16*, 449–456.

Fang, Y., Elsworth, D., Ishibashi, T., & Zhang, F. (2018). Permeability evolution and frictional stability of fabricated fractures with specified roughness. *Journal of Geophysical Research: Solid Earth*, *123*(11), 9355–9375. https://doi.org/10.1029/2018jb016215

Faulkner, D. R., Jackson, C. A. L., Lunn, R. J., Schlische, R. W., Shipton, Z. K., Wibberley, C. A. J., & Withjack, M. O. (2010). A review of recent developments concerning the structure, mechanics and fluid flow properties of fault zones. *Journal of Structural Geology*, *32*(11), 1557–1575. https://doi.org/10.1016/j.jsg.2010.06.009

Fereshtenejad, S., & Song, J.-J. (2016). Fundamental study on applicability of powder-based 3D printer for physical modeling in rock mechanics. *Rock Mechanics and Rock Engineering*, *49*(6), 2065–2074. https://doi.org/10.1007/s00603-015-0904-x

Formlabs. (2019). *Formlabs material data sheet*. Formlabs.

Gadelmawla, E. S., Koura, M. M., Maksoud, T. M. A., Elewa, I. M., & Soliman, H. H. (2002). Roughness parameters. *Journal of Materials Processing Technology*, *123*(1), 133–145. https://doi.org/10.1016/s0924-0136(02)00060-2

Gale, J. F. W., Laubach, S. E., Olson, J. E., Eichhuble, P., & Fall, A. (2014). Natural fractures in shale: A review and new observations. *Bulletin*, *98*(11), 2165–2216. https://doi.org/10.1306/08121413151

Gentier, S., Lamontagne, E., Archambault, G., & Riss, J. (1997). Anisotropy of flow in a fracture undergoing shear and its relationship to the direction of shearing and injection pressure. *International Journal of Rock Mechanics and Mining Sciences*, *34*(3–4), 94. https://doi.org/10.1016/s1365-1609(97)00085-3

Ge, S. (1997). A governing equation for fluid flow in rough fractures. *Water Resources Research*, *33*(1), 53–61. https://doi.org/10.1029/96wr02588

Glover, P. W. J., Matsuki, K., Hikima, R., & Hayashi, K. (1997). Fluid flow in fractally rough synthetic fractures. *Geophysical Research Letters*, *24*(14), 1803–1806. https://doi.org/10.1029/97gl01670

Godec, M. L., Kuuskraa, V. A., & Dipietro, P. (2013). Opportunities for using anthropogenic CO_2 for enhanced oil recovery and CO_2 storage. *Energy & Fuels*, *27*(8), 4183–4189. https://doi.org/10.1021/ef302040u

Gomez, J. S., Chalaturnyk, R., & Zambrano-Narvaez, G. (2018). Experimental investigation of the mechanical behavior and permeability of 3D printed sandstone analogues under triaxial conditions. *Transport in Porous Media*, 1–17. https://doi.org/10.1007/s11242-018-1177-0

Goodman, R. E., Taylor, R., & Brekke, T. (1968). A model for the mechanics of jointed rock. *Journal of the Soil Mechanics and Foundations Division*, *94*, 367–659. https://doi.org/10.1061/jsfeaq.0001133

Grasselli, G., Wirth, J., & Egger, P. (2002). Quantitative three-dimensional description of a rough surface and parameter evolution with shearing. *International Journal of Rock Mechanics and Mining Sciences*, *39*(6), 789–800. https://doi.org/10.1016/s1365-1609(02)00070-9

Grigoli, F., Cesca, S., Priolo, E., Rinaldi, A. P., Clinton, J. F., Stabile, T. A., et al. (2017). Current challenges in monitoring, discrimination, and management of induced seismicity related to underground industrial activities: A European perspective. *Reviews of Geophysics*, *55*(2), 310–340. https://doi.org/10.1002/2016rg000542

Hakami, E., & Larsson, E. (1996). Aperture measurements and flow experiments on a single natural fracture. *International Journal of Rock Mechanics and Mining Science & Geomechanics Abstracts*, *33*(4), 395–404. https://doi.org/10.1016/0148-9062(95)00070-4

Hale, S., Naab, C., Butscher, C., & Blum, P. (2019). Method comparison to determine hydraulic apertures of natural fractures. *Rock Mechanics and Rock Engineering*, 1–10. https://doi.org/10.1007/s00603-019-01966-7

Hasiuk, F., Ishutov, S., & Pacyga, A. (2018). Validating 3D-printed porous proxies by tomography and porosimetry. *Rapid Prototyping Journal*, *24*(3), 630–636. https://doi.org/10.1108/rpj-06-2017-0121

Head, D., & Vanorio, T. (2016). Effects of changes in rock microstructures on permeability: 3-D printing investigation. *Geophysical Research Letters*, *43*(14), 7494–7502. https://doi.org/10.1002/2016gl069334

Heindel, T. J. (2011). A review of X-ray flow visualization with applications to multiphase flows. *Journal of Fluids Engineering-Transactions of the Asme*, *133*(7). https://doi.org/10.1115/1.4004367

Hopkins, D. L. (2000). The implications of joint deformation in analyzing the properties and behavior of fractured rock masses, underground excavations, and faults. *International Journal of Rock Mechanics and Mining Sciences*, *37*(1), 175–202. https://doi.org/10.1016/s1365-1609(99)00100-8

Hopkins, D. L., Cook, N. G. W., & Myer, L. R. (1990). Normal joint stiffness as a function of spatial geometry and surface-roughness. *Rock Joints*, 203–210.

Huang, N., Liu, R., Jiang, Y., Li, B., & Yu, L. (2018). Effects of fracture surface roughness and shear displacement on geometrical and hydraulic properties of three-dimensional crossed rock fracture models. *Advances in Water Resources*, *113*, 30–41. https://doi.org/10.1016/j.advwatres.2018.01.005

Huang, Z.-Q., Winterfeld, P. H., Xiong, Y., Wu, Y.-S., & Yao, J. (2015). Parallel simulation of fully-coupled thermal-hydro-mechanical processes in CO_2 leakage through fluid-driven fracture zones. *International Journal of Greenhouse Gas Control*, *34*, 39–51. https://doi.org/10.1016/j.ijggc.2014.12.012

Huo, D., & Benson, S. M. (2015). An experimental investigation of stress-dependent permeability and permeability hysteresis behavior in rock fractures. In B. Faybishenko, S. M. Benson, & J. E. Gale (Eds.), *Fluid dynamics in complex fractured-porous systems* (pp. 99–114). https://doi.org/10.1002/9781118877517.ch7

Isakov, E., Glover, P. W. J., & Ogilvie, S. R. (2001). *Use of synthetic fractures in the analysis of natural fracture apertures* (Vol. 20, pp. 366–371). Proceedings of the 8th European Congress for Stereology and Image Analysis, Image Analysis and Stereology.

Ishibashi, T., Elsworth, D., Fang, Y., Riviere, J., Madara, B., Asanuma, H., et al. (2018). Friction-stability-permeability evolution of a fracture in granite. *Water Resources Research*, *54*(12), 9901–9918. https://doi.org/10.1029/2018wr022598

Ishibashi, T., Fang, Y., Elsworth, D., Watanabe, N., & Asanuma, H. (2020). Hydromechanical properties of 3D printed fractures with controlled surface roughness: Insights into shear-permeability coupling processes. *International Journal of Rock Mechanics and Mining Sciences*, *128*. https://doi.org/10.1016/j.ijrmms.2020.104271

Ishibashi, T., Watanabe, N., Hirano, N., Okamoto, A., & Tsuchiya, N. (2015). Beyond-laboratory-scale prediction for channeling flows through subsurface rock fractures with heterogeneous aperture distributions revealed by laboratory evaluation. *Journal of Geophysical Research: Solid Earth*, *120*(1), 106–124. https://doi.org/10.1002/2014jb011555

Ishutov, S., Hasiuk, F. J., Fullmer, S. M., Buono, A. S., Gray, J. N., & Harding, C. (2017). Resurrection of a reservoir sandstone from tomographic data using three-dimensional printing. *Bulletin*, *101*(9), 1425–1443. https://doi.org/10.1306/11111616038

Ishutov, S., Hasiuk, F. J., Harding, C., & Gray, J. N. (2015). 3D printing sandstone porosity models. *Interpretation*, *3*(3), SX49–SX61. https://doi.org/10.1190/int-2014-0266.1

Ishutov, S., Hasiuk, F. J., Jobe, D., & Agar, S. (2018). Using resin-based 3d printing to build geometrically accurate proxies of porous sedimentary rocks. *Groundwater*, *56*(3), 482–490. https://doi.org/10.1111/gwat.12601

Jaeger, J. C., Cook, N. G. W., & Zimmerman, R. (2009). *Fundamentals of rock mechanics*. Wiley.

Javanmard, H., Ebigbo, A., Walsh, S. D. C., Saar, M. O., & Vogler, D. (2021). No-Flow Fraction (NFF) permeability model for rough fractures under normal stress. *Water Resources Research*, e2020WR029080. https://doi.org/10.1007/s12351-021-00633-6

Jiang, C., & Zhao, G.-F. (2015). A preliminary study of 3D printing on rock mechanics. *Rock Mechanics and Rock Engineering*, *48*(3), 1041–1050. https://doi.org/10.1007/s00603-014-0612-y

Jiang, Q., Feng, X., Gong, Y., Song, L., Ran, S., & Cui, J. (2016). Reverse modelling of natural rock joints using 3D scanning and 3D printing. *Computers and Geotechnics*, *73*, 210–220. https://doi.org/10.1016/j.compgeo.2015.11.020

Jiang, Q., Feng, X., Song, L., Gong, Y., Zheng, H., & Cui, J. (2016). Modeling rock specimens through 3D printing: Tentative experiments and prospects. *Acta Mechanica Sinica*, *32*(1), 101–111. https://doi.org/10.1007/s10409-015-0524-4

Ju, Y., Xie, H., Zheng, Z., Lu, J., Mao, L., Gao, F., & Peng, R. (2014). Visualization of the complex structure and stress field inside rock by means of 3D printing technology. *Chinese Science Bulletin*, *59*(36), 5354–5365. https://doi.org/10.1007/s11434-014-0579-9

Kabuth, A., Dahmke, A., Beyer, C., Bilke, L., Dethlefsen, F., Dietrich, P., et al. (2017). Energy storage in the geological subsurface: Dimensioning, risk analysis and spatial planning: The ANGUS plus project. *Environmental Earth Sciences*, *76*(1). https://doi.org/10.1007/s12665-016-6319-5

Kang, P. K., Brown, S., & Juanes, R. (2016). Emergence of anomalous transport in stressed rough fractures. *Earth and Planetary Science Letters*, *454*, 46–54. https://doi.org/10.1016/j.epsl.2016.08.033

Karimzade, E., Cheraghi Seifabad, M., Sharifzadeh, M., & Baghbanan, A. (2019). Modelling of flow-shear coupling process in rough rock fractures using three-dimensional finite volume approach. *Rock Mechanics and Rock Engineering*, *52*(11), 4693–4713. https://doi.org/10.1007/s00603-019-01864-y

Ketcham, R. A., Slottke, D. T., & Sharp, J. M. (2010). Three-dimensional measurement of fractures in heterogeneous materials using high-resolution X-ray computed tomography. *Geosphere*, *6*(5), 499–514. https://doi.org/10.1130/ges00552.1

Keyence. (2017). *Digital microscope VHX-6000 user's manual*.

Klimczak, C., Schultz, R. A., Parashar, R., & Reeves, D. M. (2010). Cubic law with aperture-length correlation: Implications for network scale fluid flow. *Hydrogeology Journal*, *18*(4), 851–862. https://doi.org/10.1007/s10040-009-0572-6

Kling, T., Schwarz, J.-O., Wendler, F., Enzmann, F., & Blum, P. (2017). Fracture flow due to hydrothermally induced quartz growth. *Advances in Water Resources*, *107*, 93–107. https://doi.org/10.1016/j.advwatres.2017.06.011

Kong, L., Ostadhassan, M., Li, C., & Tamimi, N. (2018). Can 3-D printed gypsum samples replicate natural rocks? An experimental study. *Rock Mechanics and Rock Engineering*, *51*(10), 3061–3074. https://doi.org/10.1007/s00603-018-1520-3

Konzuk, J. S., & Kueper, B. H. (2004). Evaluation of cubic law based models describing single-phase flow through a rough-walled fracture. *Water Resources Research*, *40*(2). https://doi.org/10.1029/2003wr002356

Latham, J.-P., Xiang, J., Belayneh, M., Nick, H. M., Tsang, C.-F., & Blunt, M. J. (2013). Modelling stress-dependent permeability in fractured rock including effects of propagating and bending fractures. *International Journal of Rock Mechanics and Mining Sciences*, *57*, 100–112. https://doi.org/10.1016/j.ijrmms.2012.08.002

Laubach, S. E., Lamarche, J., Gauthier, B. D. M., Dunne, W. M., & Sanderson, D. J. (2018). Spatial arrangement of faults and opening-mode fractures. *Journal of Structural Geology*, *108*, 2–15. https://doi.org/10.1016/j.jsg.2017.08.008

Lepillier, B., Bruna, P.-O., Bruhn, D., Bastesen, E., Daniilidis, A., Garcia, Ó., et al. (2020). From outcrop scanlines to discrete fracture networks, an integrative workflow. *Journal of Structural Geology*, *133*, 103992. https://doi.org/10.1016/j.jsg.2020.103992

Li, B., Jiang, Y., Koyama, T., Jing, L., & Tanabashi, Y. (2008). Experimental study of the hydro-mechanical behavior of rock joints using a parallel-plate model containing contact areas and artificial fractures. *International Journal of Rock Mechanics and Mining Sciences*, *45*(3), 362–375. https://doi.org/10.1016/j.ijrmms.2007.06.004

Liu, R., He, M., Huang, N., Jiang, Y., & Yu, L. (2020). Three-dimensional double-rough-walled modeling of fluid flow through self-affine shear fractures. *Journal of Rock Mechanics and Geotechnical Engineering*, *12*(1), 41–49. https://doi.org/10.1016/j.jrmge.2019.09.002

Li, Y., & Huang, R. (2015). Relationship between joint roughness coefficient and fractal dimension of rock fracture surfaces. *International Journal of Rock Mechanics and Mining Sciences*, *75*, 15–22. https://doi.org/10.1016/j.ijrmms.2015.01.007

Li, Y., & Zhang, Y. (2015). Quantitative estimation of joint roughness coefficient using statistical parameters. *International Journal of Rock Mechanics and Mining Sciences*, *77*, 27–35. https://doi.org/10.1016/j.ijrmms.2015.03.016

Long, J. C. S., Remer, J. S., Wilson, C. R., & Witherspoon, P. A. (1982). Porous media equivalents for networks of discontinuous fractures. *Water Resources Research*, *18*(3), 645–658. https://doi.org/10.1029/wr018i003p00645

Luo, S., Zhao, Z., Peng, H., & Pu, H. (2016). The role of fracture surface roughness in macroscopic fluid flow and heat transfer in fractured rocks. *International Journal of Rock Mechanics and Mining Sciences*, *87*, 29–38. https://doi.org/10.1016/j.ijrmms.2016.05.006

Martínez, Á. R., Roubinet, D., & Tartakovsky, D. M. (2014). Analytical models of heat conduction in fractured rocks. *Journal of Geophysical Research: Solid Earth*, *119*(1), 83–98. https://doi.org/10.1002/2012jb010016

Matsuki, K., Chida, Y., Sakaguchi, K., & Glover, P. W. J. (2006). Size effect on aperture and permeability of a fracture as estimated in large synthetic fractures. *International Journal of Rock Mechanics and Mining Sciences*, *43*(5), 726–755. https://doi.org/10.1016/j.ijrmms.2005.12.001

Matsuki, K., Lee, J. J., Sakaguchi, K., & Hayashi, K. (1999). Size effect in flow conductance of a closed small-scale hydraulic fracture in granite. *Geothermal Science and Technology*, *6*, 113–138.

McCartney, J. S., Sánchez, M., & Tomac, I. (2016). Energy geotechnics: Advances in subsurface energy recovery, storage, exchange, and waste management. *Computers and Geotechnics*, *75*, 244–256. https://doi.org/10.1016/j.compgeo.2016.01.002

Méheust, Y., & Schmittbuhl, J. (2001). Geometrical heterogeneities and permeability anisotropy of rough fractures. *Journal of Geophysical Research*, *106*(B2), 2089–2102. https://doi.org/10.1029/2000jb900306

Montemagno, C. D., & Pyrak-Nolte, L. J. (1999). Fracture network versus single fractures: Measurement of fracture geometry with X-ray tomography. *Physics and Chemistry of the Earth, Part A: Solid Earth and Geodesy*, *24*(7). https://doi.org/10.1016/s1464-1895(99)00082-4

Moreno, L., Tsang, Y. W., Tsang, C. F., Hale, F. V., & Neretnieks, I. (1988). Flow and tracer transport in a single fracture: A stochastic model and its relation to some field observations. *Water Resources Research*, *24*(12), 2033–2048. https://doi.org/10.1029/wr024i012p02033

Muralidharan, V., Chakravarthy, D., Putra, E., & Schechter, D. S. (2004). *Investigating fracture aperture distributions under various stress conditions using X-ray CT scanner* (p. 14). Paper presented at the Canadian International Petroleum Conference, Petroleum Society of Canada, Calgary, Alberta. https://doi.org/10.2118/2004-230

Myers, N. O. (1962). Characterization of surface roughness. *Wear*, *5*(3), 182–189. https://doi.org/10.1016/0043-1648(62)90002-9

Nemoto, K., Watanabe, N., Hirano, N., & Tsuchiya, N. (2009). Direct measurement of contact area and stress dependence of anisotropic flow through rock fracture with heterogeneous aperture distribution. *Earth and Planetary Science Letters*, *281*(1–2), 81–87. https://doi.org/10.1016/j.epsl.2009.02.005

Nicholl, M. J., Rajaram, H., Glass, R. J., & Detwiler, R. (1999). Saturated flow in a single fracture: Evaluation of the Reynolds equation in measured aperture fields. *Water Resources Research*, *35*(11), 3361–3373. https://doi.org/10.1029/1999wr900241

Ni, X.-d., Niu, Y.-l., Wang, Y., & Yu, K. (2018). Non-darcy flow experiments of water seepage through rough-walled rock fractures. *Geofluids*, 8541421. https://doi.org/10.1155/2018/8541421

Ogilvie, S., Isakov, E., Taylor, C. W., & Glover, P. W. J. (2003). Characterization of rough-walled fractures in crystalline rocks. In N. Petford, & K. J. W. McCaffrey (Eds.), *Hydrocarbons in crystalline rocks* (pp. 125–141). Geological Society Special Publication. https://doi.org/10.1144/gsl.sp.2003.214.01.08

Olsson, R., & Barton, N. (2001). An improved model for hydromechanical coupling during shearing of rock joints. *International Journal of Rock Mechanics and Mining Sciences*, *38*(3), 317–329. https://doi.org/10.1016/s1365-1609(00)00079-4

Oron, A. P., & Berkowitz, B. (1998). Flow in rock fractures: The local cubic law assumption reexamined. *Water Resources Research*, *34*(11), 2811–2825. https://doi.org/10.1029/98wr02285

Petrovitch, C. L., Nolte, D. D., & Pyrak-Nolte, L. J. (2013). Scaling of fluid flow versus fracture stiffness. *Geophysical Research Letters*, *40*(10), 2076–2080. https://doi.org/10.1002/grl.50479

Phillips, T., Kampman, N., Bisdom, K., Forbes Inskip, N. D., den Hartog, S. A. M., Cnudde, V., & Busch, A. (2020). Controls on the intrinsic flow properties of mudrock fractures: A review of their importance in subsurface storage. *Earth-Science Reviews*, 103390. https://doi.org/10.3997/2214-4609.202021014

Piggott, A. R., & Elsworth, D. (1990). *Laboratory studies of transport within a single rock fracture rock joints* (pp. 397–404).

Piovesan, A., Achille, C., Ameloot, R., Nicolai, B., & Verboven, P. (2019). Pore network model for permeability characterization of three-dimensionally-printed porous materials for passive microfluidics. *Physical Review E*, *99*(3). https://doi.org/10.1103/physreve.99.033107

Plouraboue, F., Kurowski, P., Boffa, J. M., Hulin, J. P., & Roux, S. (2000). Experimental study of the transport properties of rough self-affine fractures. *Journal of Contaminant Hydrology*, *46*(3–4), 295–318. https://doi.org/10.1016/s0169-7722(00)00134-0

Pruess, K. (2008). Leakage of CO2 from geologic storage: Role of secondary accumulation at shallow depth. *International Journal of Greenhouse Gas Control*, *2*(1), 37–46. https://doi.org/10.1016/s1750-5836(07)00095-3

Pruess, K., & Tsang, Y. W. (1990). On two-phase relative permeability and capillary pressure of rough-walled rock fractures. *Water Resources Research*, *26*(9), 1915–1926. https://doi.org/10.1029/wr026i009p01915

Pyrak-Nolte, L. J., Cook, N. G. W., & Nolte, D. D. (1988). Fluid percolation through single fractures. *Geophysical Research Letters*, *15*(11), 1247–1250. https://doi.org/10.1029/gl015i011p01247

Pyrak-Nolte, L. J., & Morris, J. P. (2000). Single fractures under normal stress: The relation between fracture specific stiffness and fluid flow. *International Journal of Rock Mechanics and Mining Sciences*, *37*(1–2), 245–262. https://doi.org/10.1016/s1365-1609(99)00104-5

Pyrak-Nolte, L. J., Myer, L. R., Cook, N. G. W., & Witherspoon, P. A. (1987). *Hydraulic and mechanical properties of natural fractures in low permeability rock* (pp. 225–231). Proceedings of the 6th International Congress on Rock Mechanics.

Pyrak-Nolte, L. J., & Nolte, D. D. (2016). Approaching a universal scaling relationship between fracture stiffness and fluid flow. *Nature Communications*, *7*. https://doi.org/10.1038/ncomms10663

Qian, J. Z., Chen, Z., Zhan, H., & Guan, H. (2011). Experimental study of the effect of roughness and Reynolds number on fluid flow in rough-walled single fractures: A check of local cubic law. *Hydrological Processes*, *25*(4), 614–622. https://doi.org/10.1002/hyp.7849

Qian, J. Z., Zhan, H. B., Zhao, W. D., & Sun, F. G. (2005). Experimental study of turbulent unconfined groundwater flow in a single fracture. *Journal of Hydrology*, *311*(1–4), 134–142. https://doi.org/10.1016/j.jhydrol.2005.01.013

Rasmuson, A., & Neretnieks, I. (1986). Radionuclide transport in fast channels in crystalline rock. *Water Resources Research*, *22*(8), 1247–1256. https://doi.org/10.1029/wr022i008p01247

Rasouli, V., & Hosseinian, A. (2011). Correlations developed for estimation of hydraulic parameters of rough fractures through the simulation of JRC flow channels. *Rock Mechanics and Rock Engineering*, *44*(4), 447–461. https://doi.org/10.1007/s00603-011-0148-3

Raven, K. G., & Gale, J. E. (1985). Water flow in a natural rock fracture as a function of stress and sample size. *International Journal of Rock Mechanics and Mining Science & Geomechanics Abstracts*, *22*(4), 251–261. https://doi.org/10.1016/0148-9062(85)92952-3

Renard, F., Candela, T., & Bouchaud, E. (2013). Constant dimensionality of fault roughness from the scale of micro-fractures to the scale of continents. *Geophysical Research Letters*, *40*(1), 83–87. https://doi.org/10.1029/2012gl054143

Renshaw, C. E. (1995). On the relationship between mechanical and hydraulic apertures in rough-walled fractures. *Journal of Geophysical Research*, *100*(B12), 24629–24636. https://doi.org/10.1029/95jb02159

Rezaei Niya, S. M., & Selvadurai, A. P. S. (2019). Correlation of joint roughness coefficient and permeability of a fracture. *International Journal of Rock Mechanics and Mining Sciences*, *113*, 150–162. https://doi.org/10.1016/j.ijrmms.2018.12.008

Rong, G., Tan, J., Zhan, H., He, R., & Zhang, Z. (2020). Quantitative evaluation of fracture geometry influence on nonlinear flow in a single rock fracture. *Journal of Hydrology*, *589*, 125162. https://doi.org/10.1016/j.jhydrol.2020.125162

Schlüter, S., Sheppard, A., Brown, K., & Wildenschild, D. (2014). Image processing of multiphase images obtained via X-ray microtomography: A review. *Water Resources Research*, *50*(4), 3615–3639. https://doi.org/10.1002/2014wr015256

Schlische, R. W., Young, S. S., Ackermann, R. V., & Gupta, A. (1996). Geometry and scaling relations of a population of very small rift-related normal faults. *Geology*, *24*(8), 683–686. https://doi.org/10.1130/0091-7613(1996)024<0683:gasroa>2.3.co;2

Schmittbuhl, J., Gentier, S., & Roux, S. (1993). Field measurements of the roughness of fault surfaces. *Geophysical Research Letters*, *20*(8), 639–641. https://doi.org/10.1029/93gl00170

Schultz, R. A., Soliva, R., Fossen, H., Okubo, C. H., & Reeves, D. M. (2008). Dependence of displacement-length scaling relations for fractures and deformation bands on the volumetric changes across them. *Journal of Structural Geology*, *30*(11), 1405–1411. https://doi.org/10.1016/j.jsg.2008.08.001

Sharafisafa, M., Shen, L., & Xu, Q. (2018). Characterisation of mechanical behavior of 3D printed rock-like material with digital image correlation. *International Journal of Rock Mechanics and Mining Sciences*, *112*, 122–138. https://doi.org/10.1016/j.ijrmms.2018.10.012

Sharifzadeh, M., Mitani, Y., & Esaki, T. (2008). Rock joint surfaces measurement and analysis of aperture distribution under different normal and shear loading using GIS. *Rock Mechanics and Rock Engineering*, *41*(2), 299–323. https://doi.org/10.1007/s00603-006-0115-6

Skurtveit, E., Sundal, A., Bjørnarå, T. I., Soldal, M., Sauvin, G., Zuchuat, V., et al. (2020). Experimental investigation of natural fracture stiffness and flow properties in a faulted CO_2 bypass system (Utah, USA). *Journal of Geophysical Research: Solid Earth*, e2019JB018917. https://doi.org/10.1029/2019jb018917

Snow, D. T. (1969). Anisotropie permeability of fractured media. *Water Resources Research*, *5*(6), 1273–1289. https://doi.org/10.1029/wr005i006p01273

Stout, K. J. (2000). *Development of methods for the characterization of roughness in three dimensions (Ultra Precision Technology)*. Butterworth-Heinemann.

Suzuki, A., Watanabe, N., Li, K., & Horne, R. N. (2017). Fracture network created by 3-D printer and its validation using CT images. *Water Resources Research*, *53*(7), 6330–6339. https://doi.org/10.1002/2017wr021032

Tan, J., Rong, G., Zhan, H., He, R., Sha, S., & Li, B. (2020). An innovative method to evaluate hydraulic conductivity of a single rock fracture based on geometric characteristics. *Rock Mechanics and Rock Engineering*. https://doi.org/10.1007/s00603-020-02196-y

Tatone, B. S. A., & Grasselli, G. (2010). A new 2D discontinuity roughness parameter and its correlation with JRC. *International Journal of Rock Mechanics and Mining Sciences*, *47*(8), 1391–1400. https://doi.org/10.1016/j.ijrmms.2010.06.006

Tatone, B. S. A., & Grasselli, G. (2012). Quantitative measurements of fracture aperture and directional roughness from rock cores. *Rock Mechanics and Rock Engineering*, *45*(4), 619–629. https://doi.org/10.1007/s00603-011-0219-5

Thompson, M. E., & Brown, S. R. (1991). The effect of anisotropic surface roughness on flow and transport in fractures. *Journal of Geophysical Research*, *96*(B13), 21923–21932. https://doi.org/10.1029/91jb02252

Tsang, C.-F., & Neretnieks, I. (1998). Flow channeling in heterogeneous fractured rocks. *Reviews of Geophysics*, *36*(2), 275–298. https://doi.org/10.1029/97rg03319

Tsang, Y. W. (1984). The effect of tortuosity on fluid flow through a single fracture. *Water Resources Research*, *20*(9), 1209–1215. https://doi.org/10.1029/wr020i009p01209

Tsang, Y. W., & Tsang, C. F. (1989). Flow channeling in a single fracture as a two-dimensional strongly heterogeneous permeable medium. *Water Resources Research*, *25*(9), 2076–2080. https://doi.org/10.1029/wr025i009p02076

Tsang, Y. W., & Tsang, C. F. (1990). Hydrological characterization of variable-aperture fractures. *Rock Joints*, 423–431.

Tsang, Y. W., & Witherspoon, P. A. (1981). Hydromechanical behavior of a deformable rock fracture subject to normal stress. *Journal of Geophysical Research*, *86*(NB10), 9287–9298. https://doi.org/10.1029/jb086ib10p09287

Tse, R., & Cruden, D. M. (1979). Estimating joint roughness coefficients. *International Journal of Rock Mechanics and Mining Science & Geomechanics Abstracts*, *16*(5), 303–307. https://doi.org/10.1016/0148-9062(79)90241-9

Ukar, E., Laubach, S. E., & Hooker, J. N. (2019). Outcrops as guides to subsurface natural fractures: Example from the Nikanassin Formation tight-gas sandstone, Grande Cache, Alberta foothills, Canada. *Marine and Petroleum Geology*, *103*, 255–275. https://doi.org/10.1016/j.marpetgeo.2019.01.039

Unger, A. J. A., & Mase, C. W. (1993). Numerical study of the hydromechanical behavior of two rough fracture surfaces in contact. *Water Resources Research*, *29*(7), 2101–2114. https://doi.org/10.1029/93wr00516

van der Walt, S., Schonberger, J. L., Nunez-Iglesias, J., Boulogne, F., Warner, J. D., Yager, N., et al. (2014). scikit-image: Image processing in Python. *Peerj*, *2*. https://doi.org/10.7717/peerj.453

Vermilye, J. M., & Scholz, C. H. (1995). Relation between vein length and aperture. *Journal of Structural Geology*, *17*(3), 423–434. https://doi.org/10.1016/0191-8141(94)00058-8

Vlassenbroeck, J., Dierick, M., Masschaele, B., Cnudde, V., van Hoorebeke, L., & Jacobs, P. (2007). Software tools for quantification of X-ray microtomography at the UGCT. *Nuclear Instruments and Methods in Physics Research Section A: Accelerators, Spectrometers, Detectors and Associated Equipment*, *580*(1), 442–445. https://doi.org/10.1016/j.nima.2007.05.073

Vogler, D., Amann, F., Bayer, P., & Elsworth, D. (2016). Permeability evolution in natural fractures subject to cyclic loading and gouge formation. *Rock Mechanics and Rock Engineering*, *49*(9), 3463–3479. https://doi.org/10.1007/s00603-016-1022-0

Vogler, D., Settgast, R. R., Annavarapu, C., Madonna, C., Bayer, P., & Amann, F. (2018). Experiments and simulations of fully hydro-mechanically coupled response of rough fractures exposed to high-pressure fluid injection. *Journal of Geophysical Research: Solid Earth*, *123*(2), 1186–1200. https://doi.org/10.1002/2017jb015057

Vogler, D., Walsh, S. D. C., Dombrovski, E., & Perras, M. A. (2017). A comparison of tensile failure in 3D-printed and natural sandstone. *Engineering Geology*, *226*, 221–235. https://doi.org/10.1016/j.enggeo.2017.06.011

von Planta, C., Vogler, D., Chen, X., Nestola, M. G. C., Saar, M. O., & Krause, R. (2019). Simulation of hydro-mechanically coupled processes in rough rock fractures using an immersed boundary method and variational transfer operators. *Computational Geosciences*, *23*(5), 1125–1140. https://doi.org/10.1007/s10596-019-09873-0

Walsh, J. B. (1981). Effect of pore pressure and confining pressure on fracture permeability. *International Journal of Rock Mechanics and Mining Science & Geomechanics Abstracts*, *18*(5), 429–435. https://doi.org/10.1016/0148-9062(81)90006-1

Walsh, J. B., & Brace, W. F. (1984). The effect of pressure on porosity and the transport properties of rock. *Journal of Geophysical Research*, *89*(NB11), 9425–9431. https://doi.org/10.1029/jb089ib11p09425

Walsh, R., McDermott, C., & Kolditz, O. (2008). Numerical modeling of stress-permeability coupling in rough fractures. *Hydrogeology Journal*, *16*(4), 613–627. https://doi.org/10.1007/s10040-007-0254-1

Wang, G., Mitchell, T. M., Meredith, P. G., Nara, Y., & Wu, Z. (2016). Influence of gouge thickness and grain size on permeability of macrofractured basalt. *Journal of Geophysical Research: Solid Earth*, *121*(12), 8472–8487. https://doi.org/10.1002/2016jb013363

Wang, J. S. Y., Narasimhan, T. N., & Scholz, C. H. (1988). Aperture correlation of a fractal fracture. *Journal of Geophysical Research*, *93*(B3), 2216–2224. https://doi.org/10.1029/jb093ib03p02216

Wang, L., & Cardenas, M. B. (2016). Development of an empirical model relating permeability and specific stiffness for rough fractures from numerical deformation experiments. *Journal of Geophysical Research: Solid Earth*, *121*, 4977–4989. https://doi.org/10.1002/2016jb013004

Wang, M., Chen, Y.-F., Ma, G.-W., Zhou, J.-Q., & Zhou, C.-B. (2016). Influence of surface roughness on nonlinear flow behaviors in 3D self-affine rough fractures: Lattice Boltzmann simulations. *Advances in Water Resources*, *96*, 373–388. https://doi.org/10.1016/j.advwatres.2016.08.006

Watanabe, N., Hirano, N., & Tsuchiya, N. (2008). Determination of aperture structure and fluid flow in a rock fracture by high-resolution numerical modeling on the basis of a flow-through experiment under confining pressure. *Water Resources Research*, *44*(6). https://doi.org/10.1029/2006wr005411

Watanabe, N., Hirano, N., & Tsuchiya, N. (2009). Diversity of channeling flow in heterogeneous aperture distribution inferred from integrated experimental-numerical analysis on flow through shear fracture in granite. *Journal of Geophysical Research*, *114*(B4). https://doi.org/10.1029/2008jb005959

Watkins, H., Bond, C. E., Healy, D., & Butler, R. W. H. (2015). Appraisal of fracture sampling methods and a new workflow to characterise heterogeneous fracture networks at outcrop. *Journal of Structural Geology*, *72*, 67–82. https://doi.org/10.1016/j.jsg.2015.02.001

Witherspoon, P. A., Wang, J. S. Y., Iwai, K., & Gale, J. E. (1980). Validity of cubic law for fluid flow in a deformable rock fracture. *Water Resources Research*, *16*(6), 1016–1024. https://doi.org/10.1029/wr016i006p01016

Xie, L. Z., Gao, C., Ren, L., & Li, C. B. (2015). Numerical investigation of geometrical and hydraulic properties in a single rock fracture during shear displacement with the Navier-Stokes equations. *Environmental Earth Sciences*, *73*(11), 7061–7074. https://doi.org/10.1007/s12665-015-4256-3

Xiong, F., Jiang, Q., Ye, Z., & Zhang, X. (2018). Nonlinear flow behavior through rough-walled rock fractures: The effect of contact area. *Computers and Geotechnics*, *102*, 179–195. https://doi.org/10.1016/j.compgeo.2018.06.006

Xiong, X., Li, B., Jiang, Y., Koyama, T., & Zhang, C. (2011). Experimental and numerical study of the geometrical and hydraulic characteristics of a single rock fracture during shear. *International Journal of Rock Mechanics and Mining Sciences*, *48*(8), 1292–1302. https://doi.org/10.1016/j.ijrmms.2011.09.009

Yazdi, A. A., Popma, A., Wong, W., Nguyen, T., Pan, Y. Y., & Xu, J. (2016). 3D printing: An emerging tool for novel microfluidics and lab-on-a-chip applications. *Microfluidics and Nanofluidics*, *20*(3). https://doi.org/10.1007/s10404-016-1715-4

Yeo, I. W. (2001). Effect of contact obstacles on fluid flow in rock fractures. *Geosciences Journal*, *5*(2), 139–143. https://doi.org/10.1007/bf02910418

Yeo, I. W., De Freitas, M. H., & Zimmerman, R. W. (1998). Effect of shear displacement on the aperture and permeability of a rock fracture. *International Journal of Rock Mechanics and Mining Sciences*, *35*(8), 1051–1070. https://doi.org/10.1016/s0148-9062(98)00165-x

Yin, P., Zhao, C., Ma, J., & Huang, L. (2019). A unified equation to predict the permeability of rough fractures via Lattice Boltzmann simulation. *Water*, *11*(5), 1081. https://doi.org/10.3390/w11051081

Yin, P., Zhao, C., Ma, J., Yan, C., & Huang, L. (2020). Experimental study of non-linear fluid flow though rough fracture based on fractal theory and 3D printing technique. *International Journal of Rock Mechanics and Mining Sciences*, *129*. https://doi.org/10.1016/j.ijrmms.2020.104293

Yu, X., & Vayssade, B. (1991). Joint profiles and their roughness parameters. *International Journal of Rock Mechanics and Mining Science & Geomechanics Abstracts*, *28*(4), 333–336. https://doi.org/10.1016/0148-9062(91)90598-g

Zambrano, M., Pitts, A. D., Salama, A., Volatili, T., Giorgioni, M., & Tondi, E. (2019). Analysis of fracture roughness control on permeability using SfM and fluid flow simulations: Implications for carbonate reservoir characterization. *Geofluids*. https://doi.org/10.1155/2019/4132386

Zangerl, C., Evans, K. F., Eberhardt, E., & Loew, S. (2008). Normal stiffness of fractures in granitic rock: A compilation of laboratory and in-situ experiments. *International Journal of Rock Mechanics and Mining Sciences*, *45*(8), 1500–1507. https://doi.org/10.1016/j.ijrmms.2008.02.001

Zhang, Z., & Nemcik, J. (2013). Friction factor of water flow through rough rock fractures. *Rock Mechanics and Rock Engineering*, *46*(5), 1125–1134. https://doi.org/10.1007/s00603-012-0328-9

Zhou, T., & Zhu, J. B. (2018). Identification of a suitable 3D printing material for mimicking brittle and hard rocks and its brittleness enhancements. *Rock Mechanics and Rock Engineering*, *51*(3), 765–777. https://doi.org/10.1007/s00603-017-1335-7

Zhu, J. B., Zhou, T., Liao, Z. Y., Sun, L., Li, X. B., & Chen, R. (2018). Replication of internal defects and investigation of mechanical and fracture behavior of rock using 3D printing and 3D numerical methods in combination with X-ray computerized tomography. *International Journal of Rock Mechanics and Mining Sciences*, *106*, 198–212. https://doi.org/10.1016/j.ijrmms.2018.04.022

Zimmerman, R. W., Al-Yaarubi, A., Pain, C. C., & Grattoni, C. A. (2004). Non-linear regimes of fluid flow in rock fractures. *International Journal of Rock Mechanics and Mining Sciences*, *41*(3), 384. https://doi.org/10.1016/j.ijrmms.2003.12.045

Zimmerman, R. W., & Bodvarsson, G. S. (1996). Hydraulic conductivity of rock fractures. *Transport in Porous Media*, *23*(1), 1–30. https://doi.org/10.1007/bf00145263

Zimmerman, R. W., Chen, D. W., & Cook, N. G. W. (1992). The effect of contact area on the permeability of fractures. *Journal of Hydrology*, *139*(1–4), 79–96. https://doi.org/10.1016/0022-1694(92)90196-3

Zimmerman, R. W., Kumar, S., & Bodvarsson, G. S. (1991). Lubrication theory analysis of the permeability of rough-walled fractures. *International Journal of Rock Mechanics and Mining Science & Geomechanics Abstracts*, *28*(4), 325–331. https://doi.org/10.1016/0148-9062(91)90597-f

Zimmerman, R. W., & Yeo, I.-W. (2000). Fluid flow in rock fractures: From the Navier-Stokes equations to the cubic law. In B. Faybishenko, P. A. Witherspoon, & S. M. Benson (Eds.), *Dynamics of fluids in fractured rock* (Geophysical Monograph Series, pp. 213–224). https://doi.org/10.1029/gm122p0213

Zou, L., & Cvetkovic, V. (2020). Impact of normal stress-induced closure on laboratory-scale solute transport in a natural rock fracture. *Journal of Rock Mechanics and Geotechnical Engineering*, *12*(4), 732–741. https://doi.org/10.1016/j.jrmge.2019.09.006

Zou, L., Jing, L., & Cvetkovic, V. (2015). Roughness decomposition and nonlinear fluid flow in a single rock fracture. *International Journal of Rock Mechanics and Mining Sciences*, *75*, 102–118. https://doi.org/10.1016/j.ijrmms.2015.01.016